

Article

Energy-Based Design of Buckling-Restrained Steel Braced Frames for Concurrent Occurrences of Earthquake and Wind

Taonian Shan ¹ and Eric M. Lui ^{2,*}¹ Creighton Manning Engineering, 2 Winners Circle, Albany, NY 12205, USA; tashan@syr.edu² Department of Civil and Environmental Engineering, Syracuse University, Syracuse, NY 13244, USA

* Correspondence: emlui@syr.edu

Abstract: This paper describes the development of a dual hazard spectrum for use in the dynamic analysis of steel frames subject to the combined effects of earthquakes and wind. The proposed spectrum is obtained by combining the power spectra of earthquakes and wind using the square root of the sum of squares (SRSS) combination method. An equivalent time excitation function is then computed using an inverse fast Fourier transform (IFFT) and serves as input for the dynamic analysis. Using time-history analysis on the OpenSees platform, the dynamic responses expressed in terms of peak and residual inter-story and roof drifts for two multistory steel frames located in two US cities (Los Angeles and Charleston) are obtained to demonstrate that designing these buildings based on just one hazard may not be adequate. For frames that are considered under-designed, an energy-based design procedure that uses buckling-restrained braces (BRBs) to dissipate the excess energy imparted to these frames is proposed so they will satisfy the FEMA 356 recommended drift limits for the performance levels of immediate occupancy and life safety.

Keywords: earthquake–wind dual hazards; dual hazard spectrum; steel frames; buckling-restrained brace design; time-history analysis

**Citation:** Shan, T.; Lui, E.M.Energy-Based Design of Buckling-Restrained Steel Braced Frames for Concurrent Occurrences of Earthquake and Wind. *CivilEng* **2024**, *5*, 343–377. <https://doi.org/10.3390/civileng5020018>

Academic Editors: Hugo Rodrigues, Angelo Luongo and Francesco D’Annibale

Received: 26 January 2024

Revised: 22 March 2024

Accepted: 11 April 2024

Published: 15 April 2024



Copyright: © 2024 by the authors. Licensee MDPI, Basel, Switzerland. This article is an open access article distributed under the terms and conditions of the Creative Commons Attribution (CC BY) license (<https://creativecommons.org/licenses/by/4.0/>).

1. Introduction

Wind and earthquakes are two natural hazards that can cause severe damage to structures. Damage in buildings under dynamic loads can often be accounted for by examining the first few modes of vibration. High-rise buildings likely have lower frequencies in the first few modes, which make them more susceptible to damage by wind, but low-rise buildings usually have their dominant frequencies in the higher range and they are therefore mostly affected by earthquakes. As a result, current design practice often treats wind and seismic effects separately, by assuming their simultaneous occurrences are negligible. This design philosophy is reflected in ASCE/SEI 7-22 [1], where earthquake and wind load effects do not appear together in any of the load combinations used for design. However, the probability that both hazards occur concurrently does exist, especially for structures located in regions known to experience both wind and earthquake hazards, as well as for structures built near the coast. For instance, a study by Fan et al. [2] that analyzed seismic data over a 10-year period from 2006 to 2015 using the AELUMA (automated event location using a mesh of arrays) method concluded that “large storms can interact with shallow sea floor near the edge of continental shelves” and “produce seismic sources with equivalent earthquake magnitudes that can be greater than 3.5”. They called such events “stormquakes” and “found evidence of more than 10,000 stormquakes occurring from 2006 to 2019 offshore of New England, Florida and the Gulf of Mexico in the United States, as well as offshore of Nova Scotia, Newfoundland and British Columbia in Canada”.

1.1. Studies on Dual Hazards on Structures

According to [1], for structures located in regions susceptible to both earthquake and wind effects, the final design can be based on the more demanding of the two hazards in terms of the risks of exceedance for the types of limit states that are being considered in the design. Nevertheless, using probabilistic tools, Duthinh & Simiu [3] and Crosti et al. [4] showed that this approach was not always risk-consistent and indicated that structures designed for just one hazard could result in a higher risk of damage than when those same structures were designed for both earthquake and wind hazards. Duthinh & Simiu [3] used the probability of union of two disjoint events to demonstrate that risks of exceedance of limit states due to two distinct hazards could increase by a factor of up to two when compared to risks for structures exposed to only one hazard. They used an example of a water tank to demonstrate that the risk of exceedance of the limit state was greater for multi-hazards than for a single hazard. They then proposed an approach based on examining the mean return interval (MRI) of wind and earthquakes and suggested that the MRI of both hazards should be doubled to assure that risks associated with one hazard in regions where that hazard dominates were not exceeded for structures in regions where both wind and seismic hazards could occur.

Crosti et al. [4] analyzed three ten-story five-bay steel frames with different numbers of moment and shear connections using the equivalent lateral force procedure and compared the drift response of these frames under increasing load factors assigned to wind and earthquake loads. By assuming earthquakes and wind to be independent, they showed that the level of risk of achieving the same lateral drift state for a structure exposed to multiple hazards was more than twice that of the structure when it was exposed to a single hazard. They then pointed out the need to consider multi-hazard synergy in design.

Aly [5] and Aly & Abburu [6] studied earthquake and wind loads on two (54- and 76-story) high-rise reinforced concrete buildings. By performing a modal transformation of the equations of motion written for the frames and assuming Rayleigh damping for these frames, they integrated each modal equation numerically to obtain and compare the inter-story drifts. They found that when the effects of earthquakes and wind were analyzed separately, earthquakes tended to excite higher vibration modes, producing smaller inter-story drifts but higher accelerations; meanwhile, wind tended to generate larger inter-story drifts but lower accelerations. When compared to earthquakes, the accelerations due to wind lasted for a longer period and could cause occupancy discomfort. They concluded that tall buildings designed for windy conditions might be safe under moderate earthquakes but not under strong earthquakes.

Thilakarathna et al. [7] evaluated the effect of wind on the seismic performance of a 40-story dual system consisting of a reinforced concrete core wall and a special moment resisting frame. The building, which was assumed to be located in a moderate-level seismic region, was designed for three different levels of wind loads (that corresponded to low, moderate and high wind speeds). Using nonlinear time-history analysis, the inelastic seismic demand was obtained and the seismic performance under the three levels of wind loads were compared. The results showed that the levels of the design wind load had an effect on the seismic performance of the building. They concluded that in order to achieve a safe design, high-rise buildings should be analyzed for their seismic performance even if wind controlled the design.

Mazza & Vulcano [8] performed numerical analyses of five 15-story steel buildings. The first (reference) frame was a steel frame with K-bracing, and the other four were derived from the first by placing diagonal braces and/or viscoelastic dampers (VEDs) on the reference frame. A bilinear model was used for the frame members and a parallel combination of two Maxwell models and one Kelvin model was used to model the VEDs. Artificially generated accelerograms that corresponded to a medium subsoil class with different levels of peak ground accelerations were used as ground excitations. Along-wind loads in the form of time histories that correspond to a wind velocity with a return period of 5 years were generated and applied to the frames. The analyses were carried

out using a step-by-step initial stress-like iterative procedure. The results showed that to satisfactorily resist the earthquake and wind loads, both diagonal bracing and VEDs should be used.

Kwag et al. [9] proposed a framework using a risk-based multi-hazard approach. The framework uses spatial representation divided into distinct regions to combine performance functions with different intensity measures for multiple hazards. The significance of these graphically depicted regions is that they can be used to determine whether the performance of a building is governed by a single (earthquake or wind) or multiple (both earthquake and wind) hazards. Using this framework, they compared the behavior of three buildings (20-story, 30-story and 40-story high) in three locations, and demonstrated that the earthquake and wind-prone regions decreased but the multi-hazard-prone region increased with building height.

Roy et al. [10] investigated the probabilities of occurrences of low to medium earthquakes and long-duration winds in the design life of base-isolated reinforced concrete buildings, and they concluded that designing the buildings based on existing guidelines might underestimate their responses under multi-hazard excitations if damage accumulation was not considered. They formulated a multi-hazard framework using probabilistic seismic hazard analysis techniques for high-rise buildings subjected to earthquakes and long-duration winds, and they showed in their study that 20- and 25-story base-isolated high-rise reinforced concrete buildings designed for earthquakes tended to be vulnerable to wind damage.

These researchers have demonstrated that regardless of height, designing a structure to satisfy the performance criteria for a single (more dominant) hazard does not always guarantee that the performance criteria for other (less dominant) hazards will automatically be satisfied if either the wind or earthquake excitation is significant enough. More importantly, under a multi-hazard scenario, the risks of exceeding the controlling limit states are even higher. To ensure that the design is adequate, a more robust method capable of considering the concurrent occurrences of these hazards is needed.

One objective of this paper is therefore to propose a methodology by which the dual wind–earthquake hazard effect on structures can be accounted for when they are occurring simultaneously.

1.2. Buckling Restrained Braces

Both earthquakes and wind impart energy to a building. This energy needs to be dissipated if severe damage to the building is to be avoided. If a building is not equipped with any supplementary energy dissipation devices, it must undergo inelastic deformations to dissipate this energy. If the amount of inelasticity is excessive, the usefulness of the building is compromised. To limit the amount of damage, drift limits are often set for buildings of different risk categories under various performance levels [11]. To satisfy these drift limits, the use of supplementary energy dissipation devices for buildings located in high earthquake and/or strong wind regions is needed. The supplementary energy dissipation device used in the present study is a buckling restrained brace (BRB). BRBs are not only capable of dissipating energy but also provide added strength and stiffness to the structure, thereby allowing them to withstand strong earthquakes and high winds without undergoing excessive elastic and inelastic deformations.

BRBs are energy dissipation structural elements designed to yield under compression and tension. The concept of BRBs was first introduced in Japan in the late 1980s [12–14]. Since then, a number of researchers around the world have performed theoretical, experimental and numerical research on various types and configurations of BRBs. A detailed review of the research and applications of BRBs is given by Zhou et al. [15]. A typical BRB has three major components: steel core, bond-preventing layer and casing. The steel core is the axial force-resisting element of the BRB. It consists of a connection zone, a transition zone and yielding zone. The middle portion of the steel core (the yielding zone) is designed to yield under an axial force. However, the connection and transition zones are expected to remain

elastic. The bond-preventing layer decouples the casing from the core and ensures the force is carried only by the core without engaging the casing. The casing or restraining unit is often filled with concrete. Its function is to support the core and prevent it from buckling under compression; hence the name “buckling restrained brace”. Because buckling of the steel core is prevented from occurring by the concrete-filled casing, the hysteretic behavior of BRB generated through tension yielding and controlled inelastic buckling of the steel core is rather stable and plump. These inelastic deformations help dissipate energy and so frames equipped with BRBs can withstand cyclic lateral loads such as earthquakes and wind.

A second objective of this paper is to present an energy-based method to design these BRBs to dissipate the excess energy beyond what the structure itself is capable of dissipating.

2. Research Objectives

As alluded to in the preceding section, current design practice often treats wind and seismic effects separately (by assuming their simultaneous occurrence is negligible) and that the final design can be based on the more dominant of the two hazards. However, a number of researchers have demonstrated that such an approach does not always result in a safe design. Furthermore, in the design for wind, wind is often treated as a static load when its effect is dynamic in nature. The two main objectives of this research are therefore to (1) develop a methodology that can account for the dynamic effects of both wind and earthquakes acting simultaneously on structures, and (2) propose an energy-based procedure for the design of BRBs to dissipate energy from the combined hazards and ensure that the building drifts will satisfy the FEMA 356 [11] recommended drift limits.

To achieve the first objective, the proposed power spectrum is developed by combining the power spectral densities of earthquakes and wind using the square root of the sum of squares (SRSS) combination rule. This combination rule is used because it is one of most commonly used statistical approaches to account for the cumulative effect of multiple events when the probability that the maximum effect of all these events will be occurring at the same instance is not high. Applying inverse fast Fourier transform (IFFT) to this spectrum, one can obtain a time-varying excitation function which can then be used as input to the system for analysis and design.

To achieve the second objective, a simplified energy-based method developed based on the equivalent lateral force (ELF) procedure is proposed. In using this method, the energy demand is first estimated based on the target deformation and ductility that correspond to the applied excitation force. The BRBs are then designed to provide the needed energy dissipation capacity to overcome this energy demand.

Steel frames will be used in the present study because they often possess the needed ductility for earthquake-resisting designs. Furthermore, they are the type of frames that can be retrofitted relatively easily with BRBs to enhance their dynamic performance.

In performing the analyses and design described in this study, the following assumptions are used:

1. The steel frames are in an undamaged state when the dual hazards strike.
2. The excitations caused by earthquakes and wind have the same duration and their maximum effects occur within this time span, i.e., the structure is experiencing its most severe loading condition during this time interval.
3. An inherent damping of 5% of critical damping is used because this value was used by USGS to create the risk-targeted seismic maps, and these maps have been adopted for use by ASCE/SEI 7-22 [1] and IBC [16] for generating target response spectra and for use in seismic analysis and design.
4. The FEMA-recommended drift limits [11] for the performance-based seismic design (PBSD) of moment and braced steel frames are used in the present study to assess the adequacy of these frames when subject to dual wind–earthquake excitations. This is because in the proposed methodology, the dual hazard effect is represented by a time-varying excitation like that of an earthquake.

In what follows, details of methodologies used in achieving the above two objectives are provided.

3. Dual Earthquake–Wind Hazard Power Spectrum

In the present study, the dual earthquake–wind power spectrum is obtained by combining the respective earthquake and wind power spectral densities derived using earthquake and wind data given in [1,16]. The power spectral density (PSD) or power spectrum is used to represent the dual earthquake–wind effects because a power spectrum describes how the power of a time-varying signal is distributed over a range of frequencies contained in the time signal. Given both earthquakes and wind are dynamic forces, each having their own range of forcing frequencies, the effect of these frequencies on a structure having natural frequencies that fall within these frequency ranges can be accounted for together in the proposed dual power spectrum. In addition, since an energy-based approach to design is used in the present study, representing the dual hazard effect by means of a power spectrum is a rational approach to the problem.

3.1. Earthquake Power Spectrum

For earthquakes, the time series of interest is the ground acceleration $\ddot{u}_g(t)$ (in m/s^2) and its PSD (in $(\text{m/s}^2)^2/\text{Hz}$) can be computed using the equation:

$$S_{a,earthquake}(f) = \lim_{T \rightarrow \infty} \frac{1}{T} \left| \int_{-\infty}^{\infty} \ddot{u}_g(t) e^{-i(2\pi f)t} dt \right|^2 \quad (1)$$

where $i = \sqrt{-1}$ is the imaginary number, f is the frequency in Hz and T is the period in seconds.

Since $\ddot{u}_g(t)$ is not a continuous function, the integral given in Equation (1) is often carried out numerically using a fast Fourier transform (FFT).

3.2. Wind Power Spectrum

Wind is created by air movement and is dynamic in nature. Although the current design for wind effects on structures often treats wind as a static load; in actuality, wind velocity (expressed in m/s) consists of a steady (static) and a fluctuating (dynamic) component given by [17]

$$U(z, t) = \bar{U}(z) + u(z, t) \quad (2)$$

where $U(z, t)$ is the height and time-dependent wind velocity in m/s ; $\bar{U}(z)$ is the (steady) mean wind velocity in m/s at height z meters above ground; and $u(z, t)$ is the fluctuating component of wind velocity in m/s , which varies with both height z (in meters) and time t (in seconds).

The mean wind velocity in m/s at height z meters above ground can be expressed by the power law as [17]

$$\bar{U}(z) = \bar{U}(10) \left(\frac{z}{10} \right)^\alpha \quad (3)$$

where $\bar{U}(10)$ is the basic wind speed in m/s at a height of 10 m above ground [2]; $\alpha = \frac{1}{\ln\left(\frac{z_{ref}}{z_0}\right)}$ is a nondimensional parameter in which $z_0 = 1$ m is the roughness length for dense urban terrain, and $z_{ref} = 50$ m is the reference height as suggested by Holmes & Bekele [17].

Wind force is a function of wind velocity; like wind velocity, it has a steady and a fluctuating component [17], i.e.,

$$F(z, t) = \frac{1}{2} \rho C_D A U^2(z, t) \approx \frac{1}{2} \rho C_D A \bar{U}^2(z) + \rho C_D A \bar{U}(z) u(z, t) \quad (4)$$

where $F(z, t)$ is the wind force in Newtons acting at a height of z meters above ground at time t ; ρ denotes air density in kg/m^3 , and the standard value used in this study

was 1.224 kg/m^3 ; and C_D is the nondimensional drag coefficient. For a bluff body, C_D is dependent on the shape of the body [18]. If the bluff body has a rectangular cross-section with B/D (ratio of the along-wind to cross-wind dimension) larger than 2, C_D stabilizes to a value of 1.05. Since the frames used in the present study satisfy this requirement, $C_D = 1.05$ is used. A denotes the area in m^2 exposed in the along-wind direction. Note that the term that involves the square of $u(z, t)$ when Equation (2) is substituted into Equation (4) is omitted because it is relatively small when compared to the other terms.

The first term on the right side of Equation (4) represents the steady wind force which is not frequency dependent, but the second term is the force from the fluctuating wind component, which is frequency dependent and can be represented by a PSD. In the present study, the PSDs of the fluctuating wind force and acceleration are obtained as [17,19]

$$S_{f_wind}(f) = (q)^2 S_u(f) \quad (5)$$

$$S_{a_wind}(f) = \left(\frac{q}{m}\right)^2 S_u(f) \quad (6)$$

where $S_{f_wind}(f)$ denotes the PSD of the fluctuating wind force in N^2/Hz ; $S_{a_wind}(f)$ denotes the PSD of the fluctuating wind acceleration in $(\text{m/s}^2)^2/\text{Hz}$; m denotes the mass in kg; $q = \rho C_D A \bar{U}$ [17], in kg/s; and $S_u(f)$ is the PSD of the fluctuating component of wind velocity in $(\text{m/s})^2/\text{Hz}$.

A number of researchers [19–29] have proposed equations to represent $S_u(f)$. A widely used assumption for the fluctuating component of the wind velocity is a zero-mean, stationary, Gaussian random process. In the present study, the Kaimal & Finnigan [30] wind velocity spectrum was used; thus, the equation for $S_u(f)$ in $(\text{m/s})^2/\text{Hz}$ is given by:

$$S_u(f) = \sigma_u^2 \frac{22 \frac{z}{\bar{U}}}{\bar{U} \left(1 + 33 \frac{z}{\bar{U}} f\right)^{5/3}} \quad (7)$$

where f is the frequency in Hz; z is the height in meters above ground; \bar{U} is given in Equation (3); and σ_u is the standard deviation in m/s that can be calculated from $\sigma_u = I_u \bar{U}$, in which $I_u = \frac{1}{\ln\left(\frac{z}{z_0}\right)}$ is the nondimensional turbulence intensity [17].

3.3. Proposed Dual Hazard Power Spectrum

The proposed dual hazard PSD $S_{a_dual}(f)$ in $(\text{m/s}^2)^2/\text{Hz}$ is obtained by combining the PSDs of earthquakes (given by Equation (1)) and wind (given by Equation (6)) using the SRSS combination rule, i.e.,

$$S_{a_dual}(f) = \sqrt{S_{a_earthquake}^2(f) + S_{a_wind}^2(f)} \quad (8)$$

SRSS is used here because not only is it a commonly used statistical tool to combine the effects of two or more random processes when the probability that the maximum effects of these processes are occurring at the same instant is not high, it has also been successfully applied to the modal analysis of dynamic systems and used in the spectral analysis of structures subject to dynamic excitations. The reason that the power spectral densities of the two hazards are combined using SRSS as opposed to just combining the results of structural responses to each of the two hazards is because the response, and in particular the inelastic response, of the structure will be more accurately captured if the combined energies of the two hazards are applied concurrently to the structure.

Once the dual hazard power spectrum is obtained from Equation (8), the dual hazard acceleration time-history can be generated using the inverse fast Fourier transform (IFFT). In using IFFT, a phase angle needs to be defined. In the present study, the phase angle used to generate this dual hazard acceleration time-history is taken as the same as that of the input earthquake data since it is not rational to employ a random phase angle which

will lead to a time series that may not be compatible with the original ground motion phase angle.

The steady wind component can now be combined with the fluctuating component in the time domain, as follows:

$$A_{dual} = a_{dual} \pm \bar{a}_{wind} \quad (9)$$

where A_{dual} is the total dual hazard excitation (in m/s^2); a_{dual} is the dual hazard acceleration (in m/s^2) that corresponds to the fluctuating part of the wind load; and $\bar{a}_{wind} = \frac{1}{2} \rho C_D A \bar{U}^2(z) / m$ (in m/s^2) is the dual hazard acceleration caused by the steady part of the wind load. The plus or minus sign in Equation (9) accounts for the possibility that wind can blow in either direction, and so the steady wind component is added to or subtracted from the fluctuating component, in order to determine the more severe condition for the analysis.

The flow chart in Figure 1 summarizes the steps needed for the construction of this proposed dual hazard power spectrum and the generation of a time-domain dual hazard excitation function. Once this function is obtained, time history analysis can be carried out on the system.

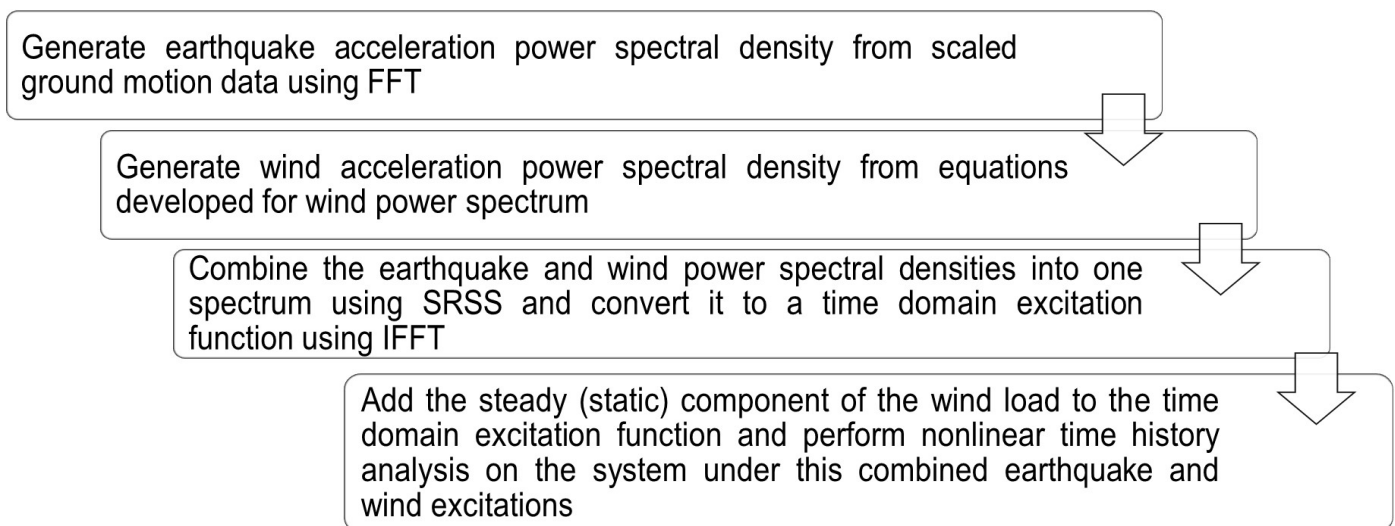


Figure 1. Procedure of generating the dual earthquake–wind hazard power spectrum and time domain excitation function.

4. Earthquake and Wind Data Characterizations

To apply the dual hazard methodology to a structure, the structure’s location and performance levels must be known so that the appropriate earthquake and wind data can be gathered and utilized. In the present study, high occupancy (or risk category III) buildings located in Los Angeles (California) and Charleston (South Carolina) are used. Both Los Angeles and Charleston are located in earthquake-prone regions of the US that are also subject to high wind [1,16]. Earthquakes are considered the more dominant hazard in Los Angeles while wind is considered more dominant in Charleston, although both earthquakes and wind are regarded as important natural hazards in both cities. Because they are both coastal cities (one on the west coast and the other on the east coast of the US), they are also susceptible to stormquakes.

According to [1], risk category III structures are defined as structures which “represent a substantial hazard to human life in the event of failure”. These structures represent the majority of structures built in these two cities. Risk category III buildings are required to be designed for immediate occupancy (IO) under design based earthquakes (DBEs) and for life safety (LS) under maximum considered earthquakes (MCEs). DBEs and MCEs have a 10% and 2% probability of exceedance over a period of 50 years, with mean return periods of 475 and 2475 years, respectively. The engineering demand parameters (EDP) that

can be used to quantify the performances of buildings are peak (maximum) and residual (permanent) drifts. According to [11], the drift ratios (lateral displacement divided by height) for steel moment and braced frames designed for IO and LS should not exceed the limits given in Table 1. Since the drift limits are different for the two performance levels, time-history analyses will be performed for both.

Table 1. Drift limits for IO and LS [11].

Steel Frame Type	Immediate Occupancy (IO)		Life Safety (LS)	
	Peak Drift	Residual Drift	Peak Drift	Residual Drift
Moment frames	0.7%	Negligible	2.5%	1%
Braced frames	0.5%	Negligible	1.5%	0.5%

4.1. Earthquake Data

According to [1], the soil site for Los Angeles is Class CD (dense sand or very stiff clay with an estimated shear wave velocity between 305 and 442 m/s) and that for Charleston is Class DE (loose sand or medium stiff clay with an estimated shear wave velocity between 152 and 213 m/s). Based on these soil site classifications, 24 ground motion records (12 for each site, as shown in Tables A1 and A2 of Appendix A) were selected. Before analysis can be carried out, these ground motions need to be scaled against a site-specific target spectrum. The DBE (for the performance level of IO) and MCE (for the performance level of LS) target spectra used for scaling the selected ground motions for Los Angeles and Charleston can be obtained from [1] or from <https://asce7hazardtool.online> (accessed on 15 August 2023) and are shown in Figure 2. Note that all the ASCE/SEI 7-22 spectra assume a 5% damping, and the MCE spectra are obtained from the respective DBE spectra by multiplying the ordinates of the latter by 1.5. The software SeismoMatch (<https://seismosoft.com/products/seismomatch>) (accessed on 15 August 2023) can be used for this scaling. Once the ground motions have been scaled, Equation (1) can be used to develop the earthquake power spectra.

4.2. Wind Data

To keep the probability of exceedance consistent for both earthquakes and wind for the performance levels of IO and LS, the probability of exceedance for wind is calculated based on a Poisson distribution given by

$$P = \frac{\left(\frac{t}{T}\right)^x e^{-\frac{t}{T}}}{x!} \quad (10)$$

where P is the probability of exceedance over a period of t years, T is the mean return period in years and x is the number of occurrences in t years.

For a given location, the mean return period (or mean recurrence interval) of wind at each performance level can be estimated using the wind maps given in [1] or from <https://asce7hazardtool.online> (accessed on 1 September 2023). The basic wind speeds $\bar{U}(10)$ determined at the two locations (Los Angeles and Charleston) for the two performance levels (IO and LS) are given in Table 2. Equations (6) and (7) can now be used to obtain the wind power spectra.

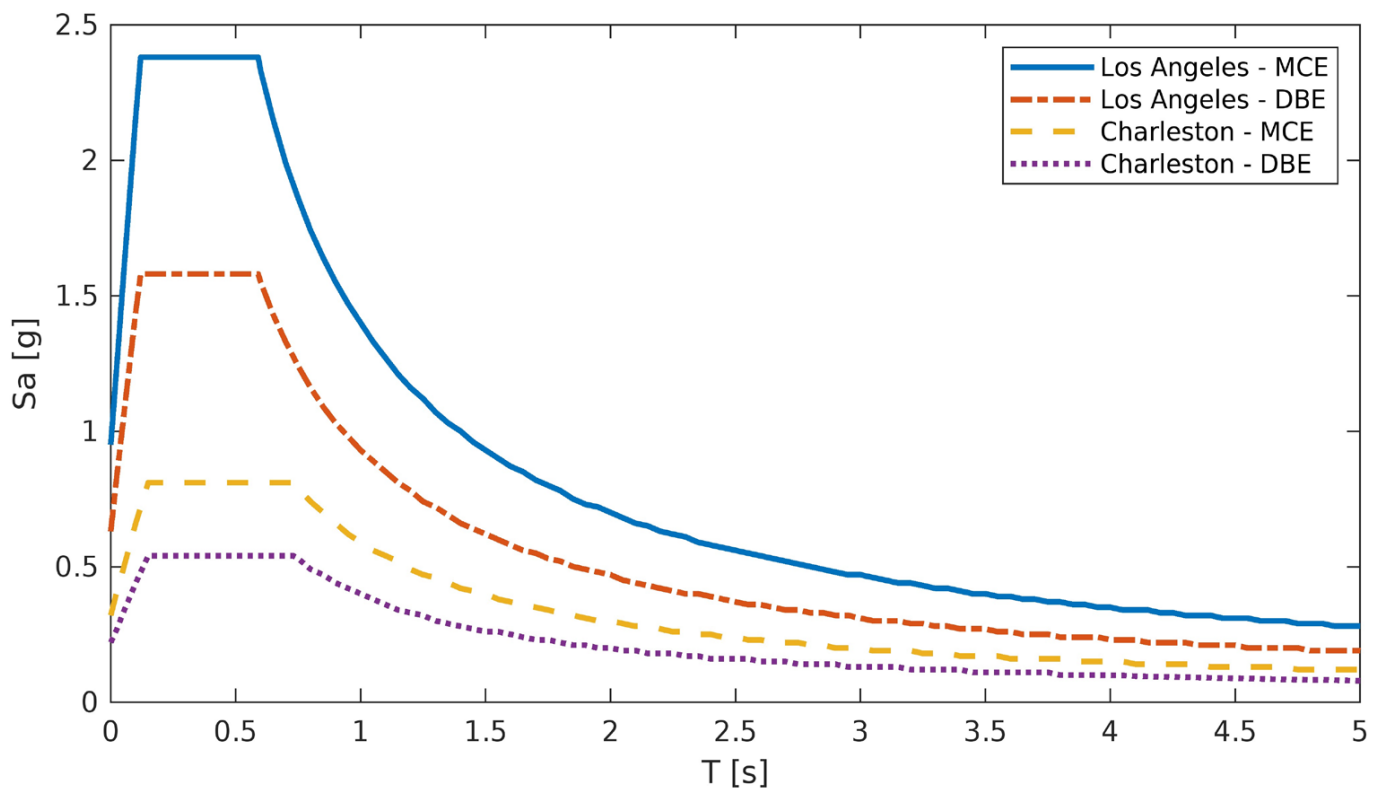


Figure 2. Target spectra (5% damping).

Table 2. Basic wind speed (in m/s) at 10 m above ground.

	Los Angeles	Charleston
Immediate Occupancy (IO)	41	62
Life Safety (LS)	46	72

5. Dual Earthquake–Wind Hazard Excitations

For each earthquake and wind load, the dual earthquake–wind power spectrum is obtained by combining the earthquake and wind power spectra using Equation (8). The dual earthquake–wind excitation A_{dual} is then obtained by first determining a_{dual} by applying an inverse fast Fourier transform (IFFT) to the dual earthquake–wind power spectrum, then adding or subtracting the steady component of wind \bar{a}_{wind} in accordance with Equation (9).

As an illustration, the power spectrum computed for a ground motion with a record sequence number (RSN) of 725 (Table A1), scaled using the response spectrum for the performance level of IO in Los Angeles, is shown in Figure 3a. The corresponding power spectrum for wind—using a basic wind speed of 41 m/s and applied to a hypothetical portal frame with 3.96 m height, 18 m² along-wind surface area and 21,000 kg mass—is shown in Figure 3b. By using Equation (8), the dual earthquake–wind power spectrum is shown in Figure 3c. Applying IFFT to this spectrum and incorporating the steady component of wind using Equation (9), the resulting dual earthquake–wind excitations are shown in Figure 3d. Note that the plus and minus signs in Equation (9) lead to two excitations: one with \bar{a}_{wind} added to and one with \bar{a}_{wind} subtracted from a_{dual} . Therefore, for a given structure, two analyses need to be performed to determine which would result in a more severe condition.

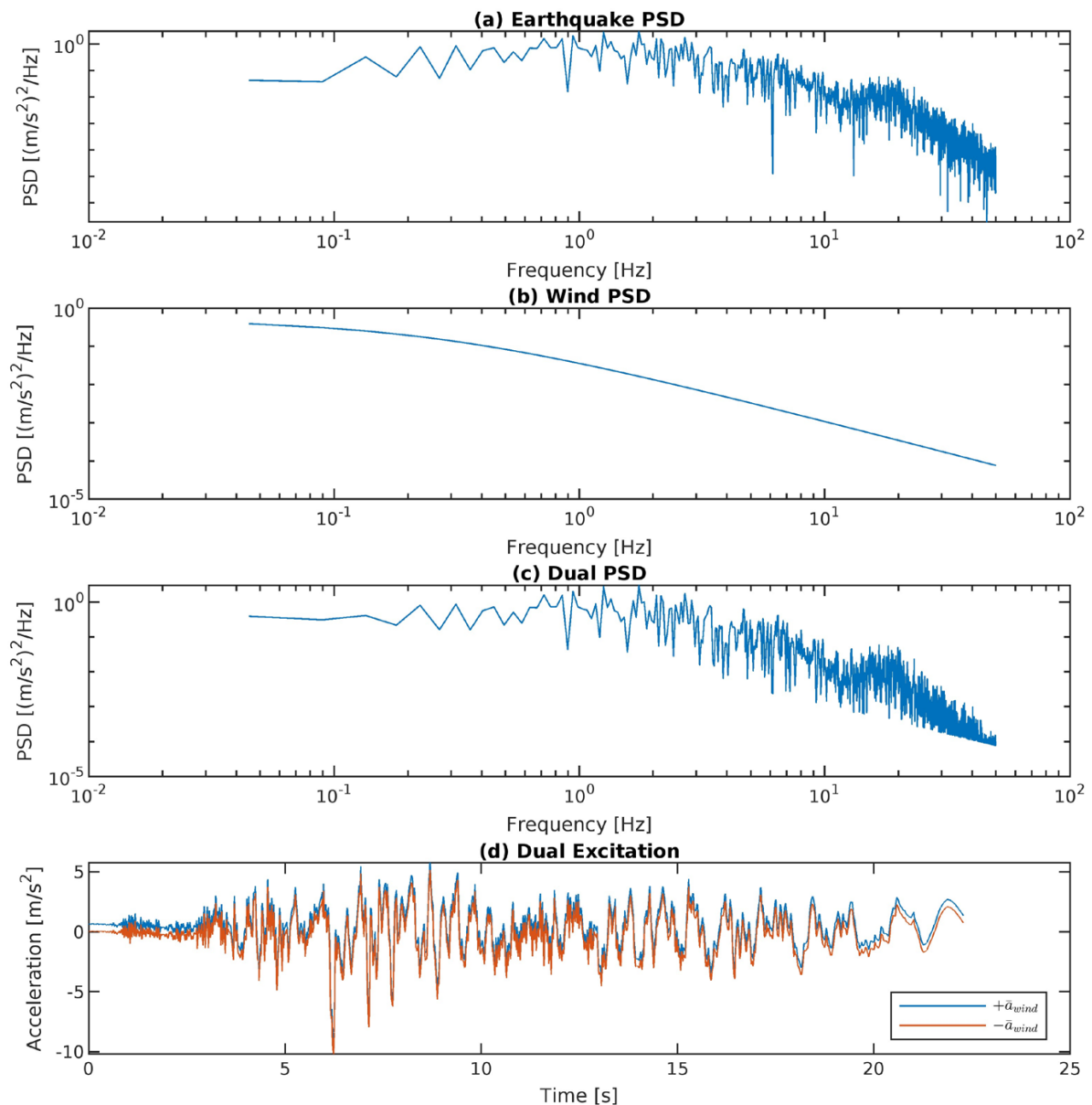


Figure 3. (a) Power spectrum of a scaled earthquake (RSN 725), (b) power spectrum for wind with 41 m/s basic wind speed, (c) dual earthquake–wind power spectrum and (d) dual earthquake–wind excitations for the performance level of IO in Los Angeles.

6. Analysis Results for Moment Resisting Frame Responses to Dual Earthquake and Wind Hazards

The dual earthquake–wind excitations will now be applied to two steel frames. A three-story and a nine-story moment resisting frame (MRF) representing the typical low- and mid-rise buildings are to be analyzed. These frames were part of a study in the SAC Joint Venture [31]. The SAC Joint Venture was formed in mid-1994 with the specific goal of “investigating the damage to welded steel moment frame buildings in the 1994 Northridge earthquake and developing repair techniques and new design approaches to minimize damage to steel moment frame buildings in future earthquakes”. The frames designed and reported in this SAC project have since been used by a number of researchers as benchmark structures in their study of the dynamic responses of steel buildings. Detailed descriptions of these steel frames can be found in [31]. It should be noted that all the beams and columns used for these two frames are compact sections, so local buckling of flanges and webs will

not occur though nonlinearities in the form of the P-delta effect and inelasticity will be considered in all the analyses.

Both frames were modeled as 2-D structures with three degrees of freedom per node using OpenSees (<https://opensees.berkeley.edu>) (accessed on 15 August 2023). To allow modeling of geometrical and material nonlinearities, nonlinear beam–column elements with fiber sections were used to model the columns and beams. Each member was discretized into 6 segments and the cross-sections of the W-shaped columns and beams were discretized into 48 fibers, with 2 layers of 8 fibers used for both the flanges and the web to capture the progression of inelastic behavior along the member and over the cross-section. The commonly used Steel01 material was used to represent the frame material with a bilinear and kinetic hardening ratio of 0.003. The elastic modulus is 200 GPa (29,000 ksi) and the design yield strengths for the beams and columns are 248 MPa (36 ksi) and 345 MPa (50 ksi), respectively. Seismic lumped masses were transferred from the beam to the floor level nodes. The base of the frames was modeled as fixed for the 3-story frame but pinned for the nine-story frame. Although the nine-story frame has a basement, the lateral translation at the ground level was restrained so the translations at the ground and basement levels were considered negligible. In this study, only the responses of the frames above ground were investigated. To avoid bi-axial bending, the moments at the end of one of the exterior bays for the nine-story frame were released.

Gravity load was incorporated in OpenSees to allow for the P-delta effect of gravity load from all the interior frames to be considered in the analysis. The gravity load consisted of two parts. One was from the tributary area associated with each moment resisting frame and was applied as vertically distributed load on the beams. The other was from the tributary area associated with the interior gravity frames and was applied to each story on a leaning column placed on one side of the moment frame and connected via rigid links to the frame. The axial loads applied to this leaning column were used to simulate the P-delta effect caused by gravity loads acting on these interior frames. The rigid links were modeled as truss elements. The leaning columns were modeled as very stiff elastic beam–column elements with pinned connections at the floor level. These leaning columns have no effect on the lateral stiffness of the moment frames. The pinned connection was modeled as a rotational spring with very small stiffness.

Since the power spectrum of wind changes with height, the dual excitations computed using the methodology described in the previous sections are story based. Each story is subject to a different time-history excitation applied to mass points of that story. All beam-to-column joints are considered mass points where the seismic lumped masses are placed. Figure 4 shows how the excitations vary from story to story for the three-story MRF.

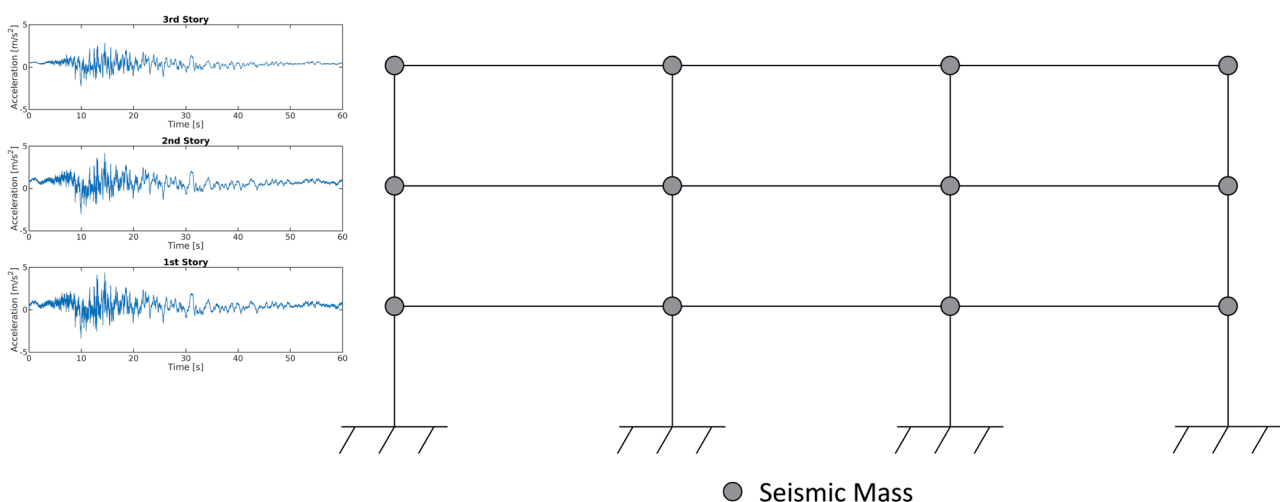


Figure 4. Story-based time-history excitations and seismic lumped masses used for the three-story MRF.

The analysis was performed using the Newton algorithm and the Newmark-beta method with a tolerance of 10^{-6} . Rayleigh damping was used, with a damping ratio of 5% assigned to the first and third modes of the structure. A 5% damping was used because the target spectra shown in Figure 2 and used to scale the ground motions were all based on 5% damping. Another 20 s zero excitation was added to the time-history loading, in order to capture the frame response after the dynamic excitation ceases.

6.1. Three-Story Frame

The analysis results for the peak and residual inter-story and roof drift ratios of the three-story frame subject to the 12 earthquake, wind and dual excitations in Los Angeles and Charleston are summarized in Figures 5–8. The vertical lines in the figures represent the mean values of the 12 responses obtained using nonlinear time-history analysis, with earthquake responses shown by red circles, wind responses shown by blue squares, and dual responses shown by green diamonds. The standard deviations, shown in the form of error bars, were computed to show the variability or spread of the analysis results.

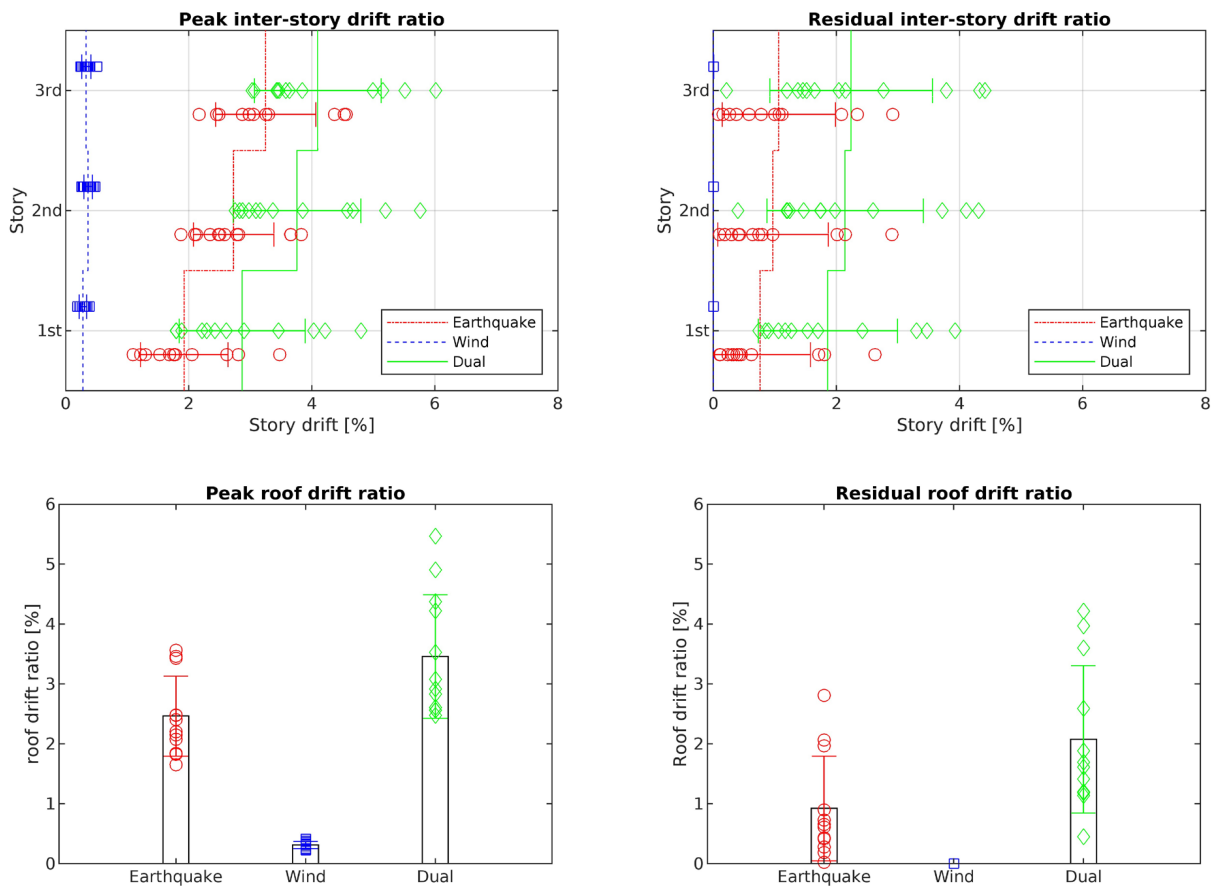


Figure 5. Peak and residual inter-story and roof drift ratios of the three-story MRF in Los Angeles, analyzed for IO.

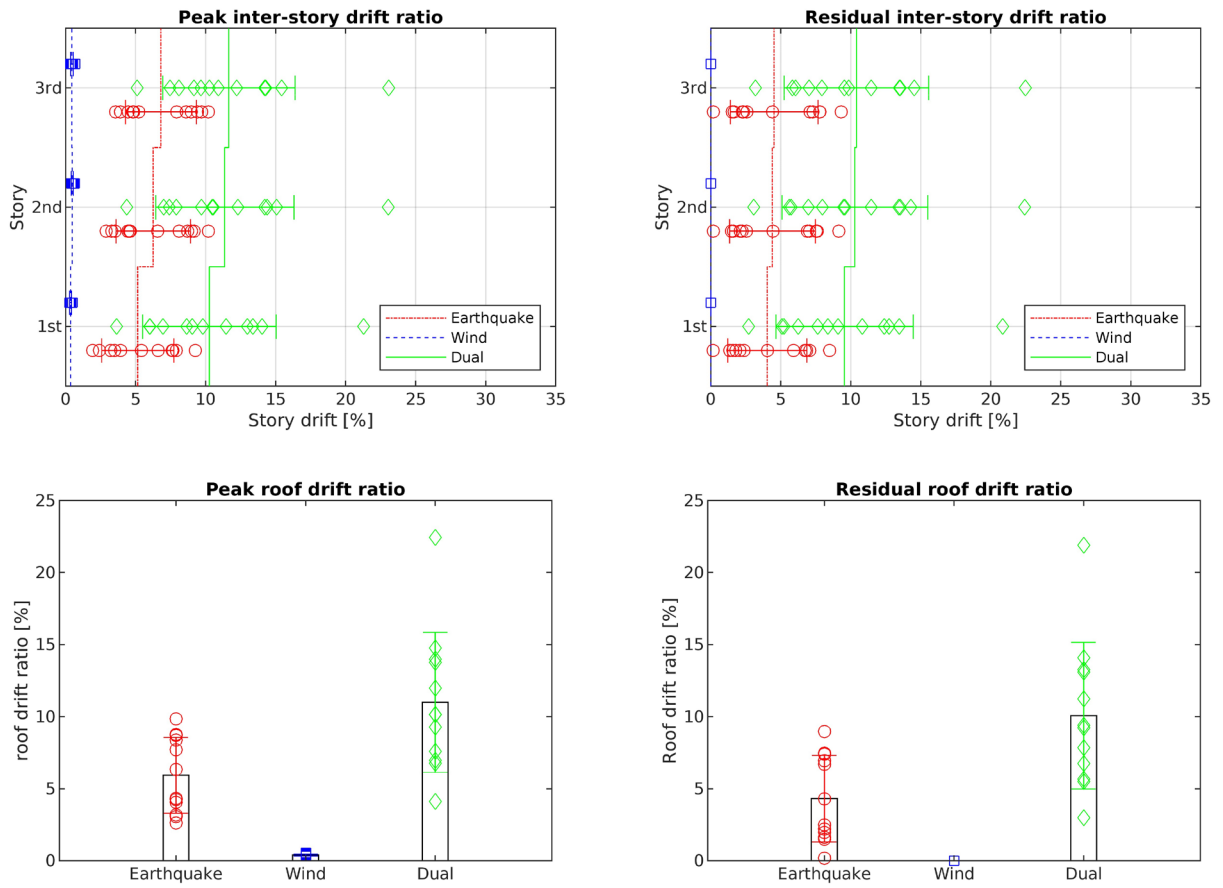


Figure 6. Peak and residual inter-story and roof drift ratios of the three-story MRF in Los Angeles, analyzed for LS.

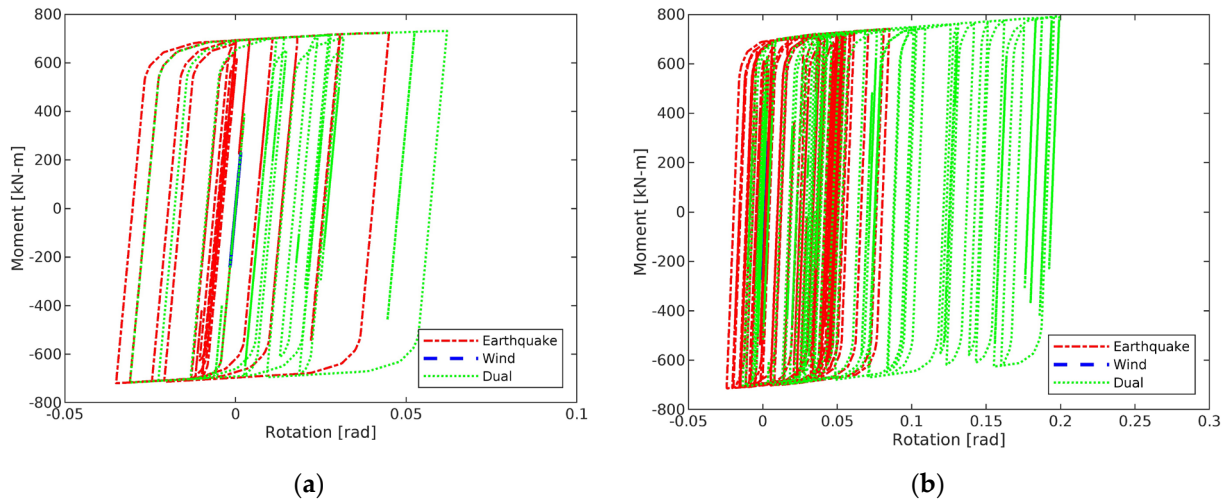


Figure 7. Hysteresis curves of a third story beam for the three-story frame in Los Angeles under the performance level of (a) IO and (b) LS.

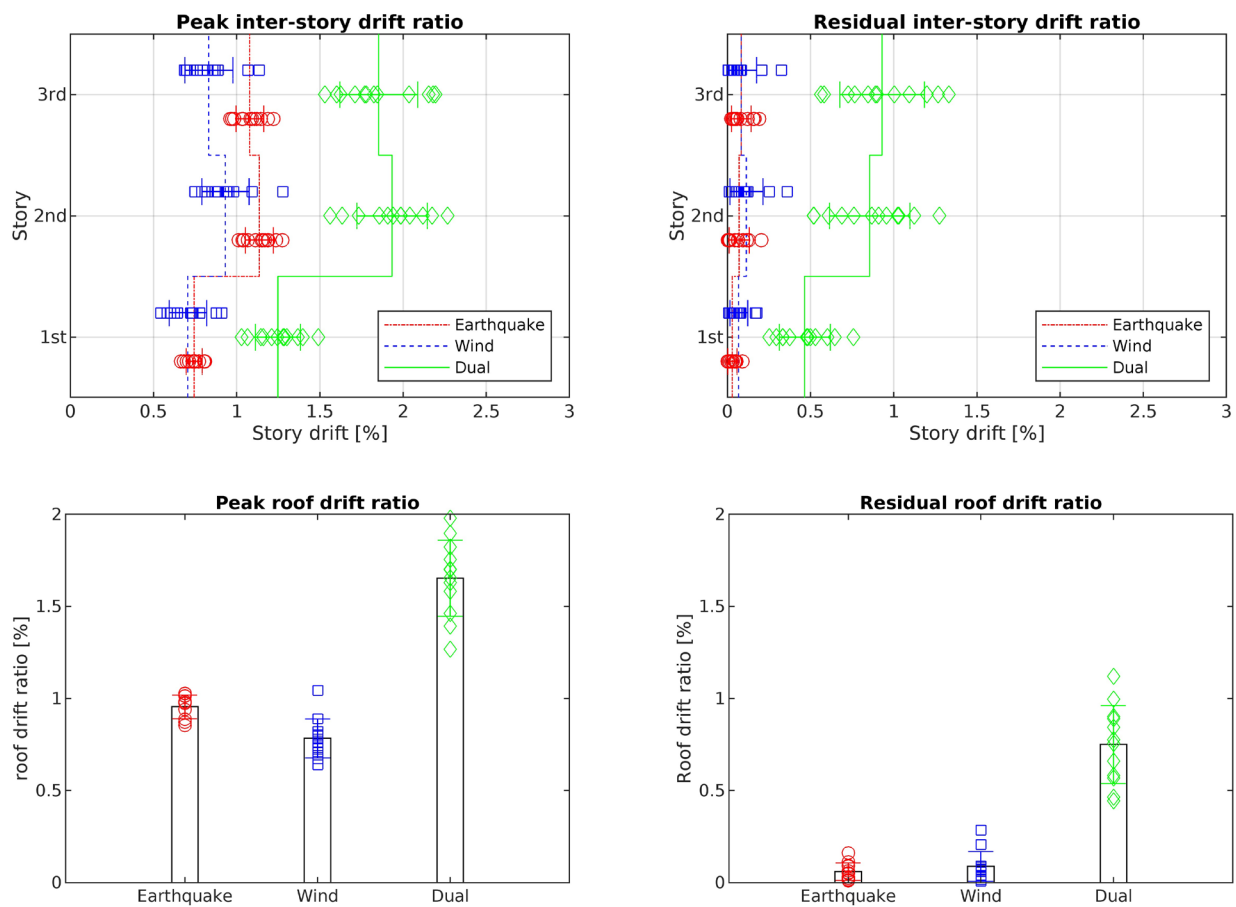


Figure 8. Peak and residual inter-story and roof drift ratios of the three-story MRF in Charleston, as analyzed for IO.

Los Angeles:

Figure 5 shows the peak and residual inter-story and roof drift ratios of the three-story frame analyzed for IO in Los Angeles. The structure experienced a maximum mean peak inter-story drift of 3.25% in the top story due to earthquakes, 0.36% in the middle story due to wind, and 4.10% in the top story due to the dual excitations. The corresponding maximum mean residual inter-story drift ratios were 1.06%, 0% and 2.24%, respectively. As for the peak and residual roof drifts, the mean values were 2.47%, 0.31% and 3.46%, and 0.92%, 0% and 2.08% due to earthquake, wind and dual excitations, respectively.

When the frame was analyzed for LS in Los Angeles, it can be seen from Figure 6 that the structure experienced maximum mean peak inter-story drift ratios of 6.80%, 0.47% and 11.65% and maximum mean residual inter-story drift ratios of 4.52%, 0% and 10.40% due to earthquake, wind and dual excitations, respectively.

The mean peak and residual roof drift ratios were 5.94% and 4.32% under earthquakes, 0.40% and 0% under wind, and 10.99% and 10.08% under the dual excitations.

The results for this three-story frame in Los Angeles show that earthquakes are the more predominant hazard. Although wind itself does not cause any damage to the frame, the combined excitation indicates that the frame experiences deformations much larger than those subject to earthquakes only. If the structure is analyzed separately for these two hazards, the sum of the peak or residual responses cannot accurately represent the response of the combined excitation effect. After the structure experiences yielding, inelastic deformations will increase rapidly with the applied forces. To illustrate this, the moment-rotation hysteresis curves of a third-story beam for one typical loading case are shown in Figure 7. The increase in inelasticity due to the combined effects of wind and earthquake is clearly seen. This story is selected because from Figures 5 and 6 it can be seen that this

story experiences the largest story and roof drifts. Using the FEMA 356 drift limits given in Table 1, the frame is not considered satisfactory for either the IO or LS performance level.

Charleston:

When the frame was analyzed for IO in Charleston, it can be seen from Figure 8 that the largest mean peak inter-story drift ratios occurred in the middle story and were equal to 1.14% under earthquakes, 0.93% under wind and 1.93% under the dual excitations. The largest mean residual inter-story drift ratios occurred in the upper stories and were equal to 0.083% under earthquakes, 0.11% under wind and 0.93% under the dual excitations.

The peak roof drift ratios were 0.96% under earthquakes, 0.78% under wind, and 1.65% under the dual excitations, while the corresponding residual roof drift ratios were 0.06%, 0.09% and 0.75%.

When the frame was analyzed for LS, Figure 9 shows that the frame in Charleston experienced maximum mean peak inter-story drift ratios of 1.75% in the top story under earthquakes, 1.35% in the middle story under wind and 3.57% in the middle story under the dual excitations. The maximum mean residual inter-story drifts were 0.32% in the top story under earthquakes, 0.42% in the middle story under wind, and 2.62% in the top story under the dual excitations. The mean peak and residual roof drift ratios were 1.39% and 0.24%, 1.14% and 0.36%, and 3.27% and 2.42% under earthquake, wind and dual excitations, respectively.

The results obtained for this three-story frame illustrate the importance of performing dual hazard design. When analyzed for LS, the frame is considered adequate when subject only to either earthquake or wind excitation. However, under the dual excitations, the frame's responses are shown to have fallen outside the range of acceptability for both the inter-story and roof drift ratios. This is the result of an increase in inelastic deformations (as illustrated in Figure 10), where the hysteresis curves of a third-story beam for one typical loading case under the performance levels of IO and LS are shown. The inelastic response of the frame subject to the dual earthquake–wind excitations is seen to be larger than the sum of the earthquake and wind responses. This means that even if separate designs were performed for earthquake and wind only and the results were summed together, the structure would still potentially undergo damage when both hazards occur concurrently.

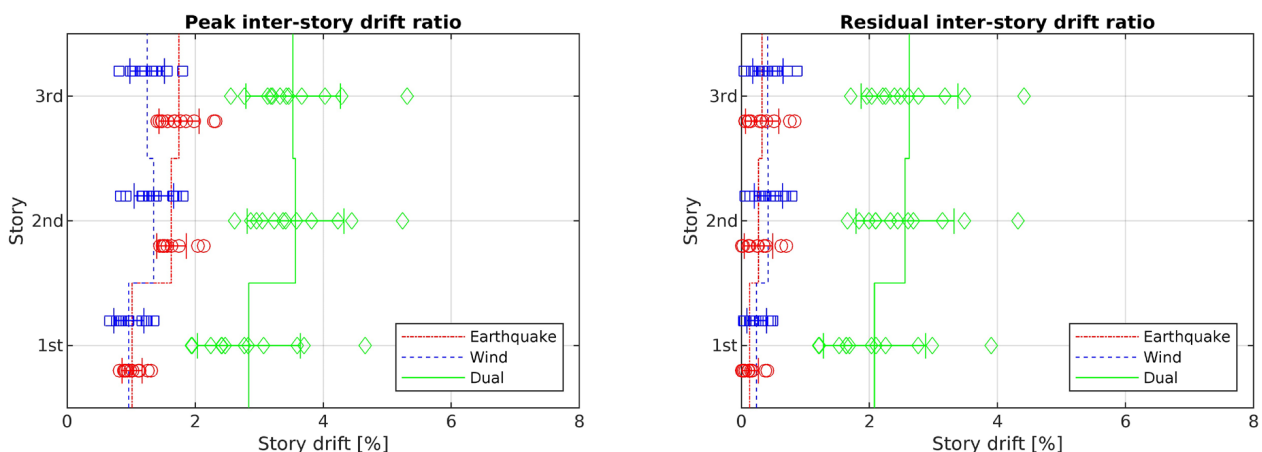


Figure 9. Cont.

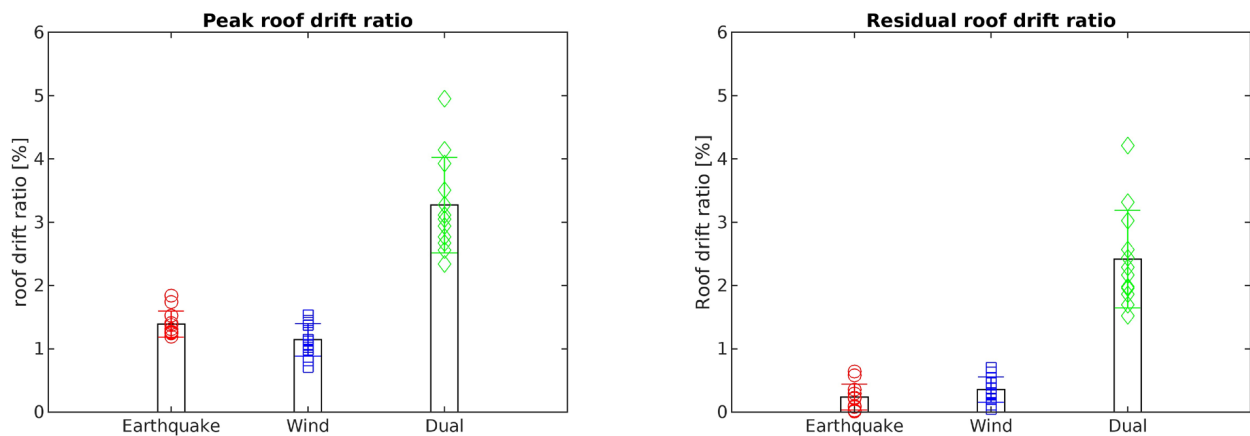
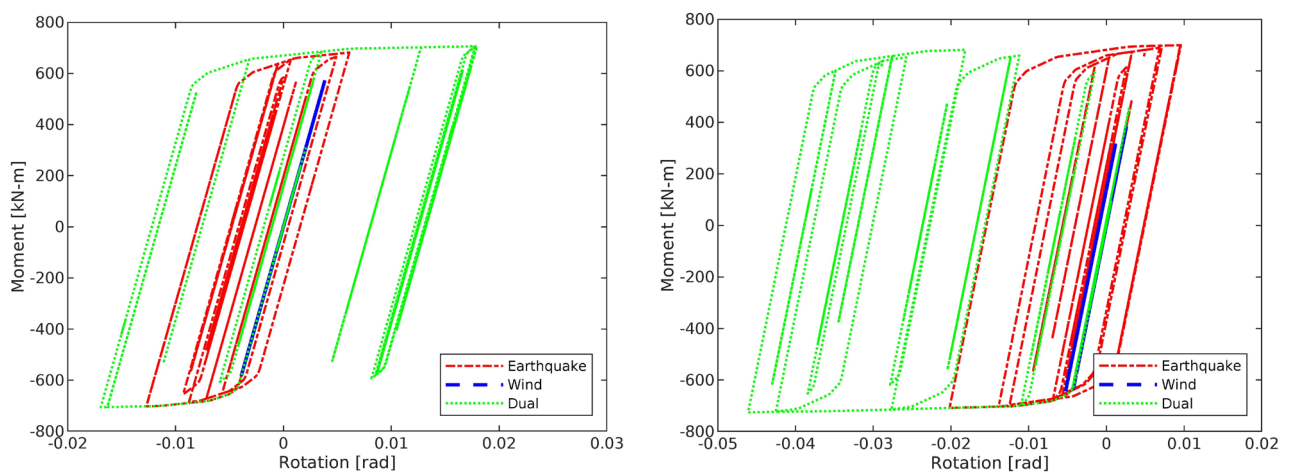


Figure 9. Peak and residual inter-story and roof drift ratios of the three-story MRF in Charleston, as analyzed for LS.



(a)

(b)

Figure 10. Hysteresis curves of a third-story beam for the three-story frame in Charleston under the performance level of (a) IO and (b) LS.

6.2. Nine-Story Frame

The nine-story frame was analyzed to demonstrate how the dual hazard effect would impact a typical mid-rise building. The analyses showed that this nine-story building in Los Angeles and Charleston would experience unacceptably large inelastic deformations under the dual excitations.

Los Angeles:

The frame located in Los Angeles could withstand earthquake or wind only, but under the dual excitations the mean peak and residual inter-story drifts became unsatisfactorily large for the performance level of IO, as shown in Figure 11. The maximum mean peak inter-story drift ratio was 2.52% in the third story under earthquakes, but it was only 0.77% in the first story under wind. The corresponding residual inter-story drift ratios were 1% under earthquakes and almost negligible under wind. However, the largest mean peak and residual inter-story drift ratios were 10.4% and 9.83% in the second story under the dual excitations. These inter-story drifts far exceeded those presented in Table 1. The mean peak roof drift ratios for this nine-story frame were 1.82% under earthquakes and 0.61% under wind load. The mean residual roof drift ratios were 0.74% under earthquakes and

negligible under wind. However, the mean peak and residual roof drift ratios increased to 6.72% and 6.19% under the dual excitations.

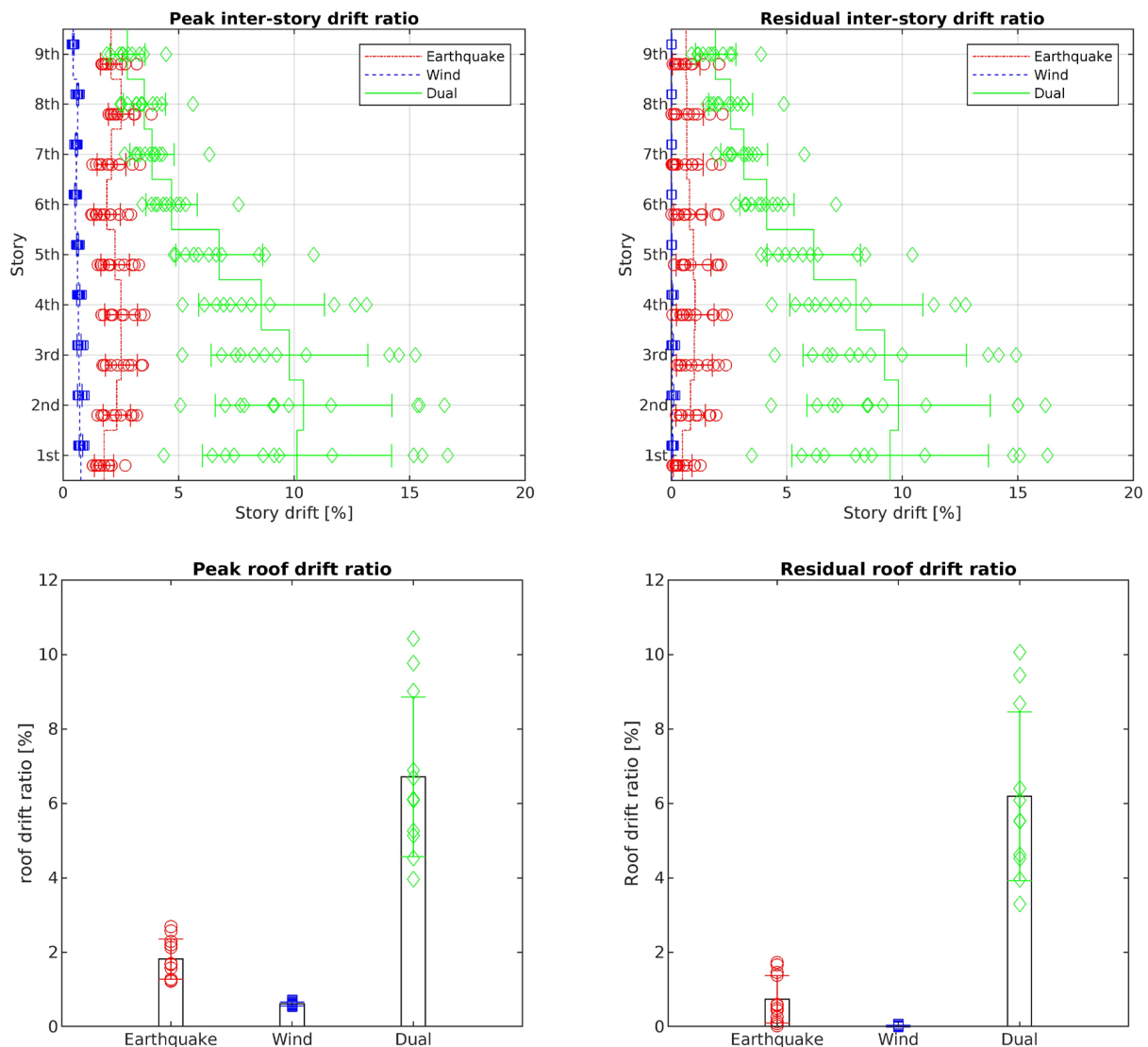


Figure 11. Peak and residual inter-story roof drift ratios of the nine-story MRF in Los Angeles, as analyzed for IO.

The noticeable increase in inter-story and roof drifts was the result of inelasticity. This is illustrated in Figure 12, where the moment–rotation hysteresis curves of a second-story beam under a typical loading case are shown. The second story was selected because it experienced the largest story drifts, as shown in Figure 11. As can be seen, the beam experienced much larger inelastic deformations under the dual loading than under just the earthquake or wind loading.

When analyzed for LS, the mean peak inter-story, residual inter-story, peak roof and residual roof drift ratios under earthquake excitation were 4.36%, 2.83%, 3.20% and 2.19%, respectively; under wind excitation, they were 1.08%, 0.35%, 0.78% and 0.14%. However, when analyzed for dual excitations, extremely large frame deflections occurred that resulted in a convergence problem for the frame. Note that this convergence problem occurred only when the full value of the excitation was used. No convergence problem was experienced when a reduced value of the excitation was used. From the results shown in Figure 11, it can be seen that wind by itself does not significantly contribute to the response of the frame but it increases the risk of structural failure due to excessive deformations when acting in

conjunction with earthquakes, as inelastic deformations are exacerbated. Knowing that the effect of wind becomes more important as the height of the building increases, its effect on buildings—especially when combined with other hazards such as earthquakes—should be carefully taken into consideration even in regions of low wind hazard.

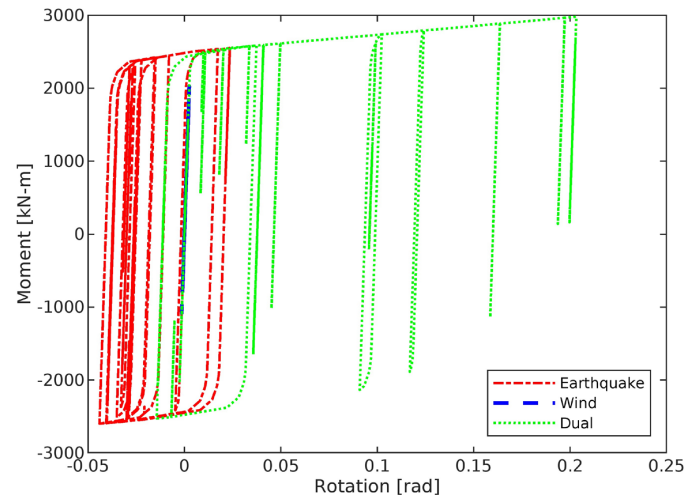


Figure 12. Hysteresis curves of a second-story beam for the nine-story frame in Los Angeles under the performance level of IO.

Charleston:

When the frame in Charleston was analyzed for IO, the mean peak inter-story, residual inter-story, peak roof and residual roof drift ratios under earthquake excitation were determined to be 1.30%, 0.16%, 0.84% and 0.08%, respectively; under wind excitation, these values increased to 9.40% 8.70%, 4.92% and 4.38%. Under the dual excitations, the drift ratios were excessively large such that convergence became a problem in the analysis.

When the frame was analyzed for LS, the mean peak inter-story, residual inter-story, peak roof and residual roof drift ratios under earthquake excitation were 1.71%, 0.42%, 1.18% and 0.26%, respectively. However, excessively large deflections (that caused convergence problems) were encountered when the frame was analyzed for wind and dual excitations. The frame was therefore considered unsatisfactory under these loading conditions.

7. Modeling of Buckling-Restrained Braces

For frames that exceed the FEMA 356 [11] recommended drift limits given in Table 1, supplementary energy dissipation devices can be added to the MRFs. In this study, buckling-restrained braces (BRBs) were used.

In the present research, BRB was modeled in OpenSees using a corotational truss element with a Steel4 material. Table 3 shows the parameters of this Steel4 material model used in the present study. The parameters were similar to those used in the Menegotto and Pinto [32] model, which was later modified and extended by Filippou et al. [33]. These parameters were calibrated by Zsarnóczy & Baker [34] and modified to match the cyclic response of BRBs modeled using Steel02 and Pinching4 materials by Upadhyay et al. [35] and the experimental data reported by Xu & Pantelides [36].

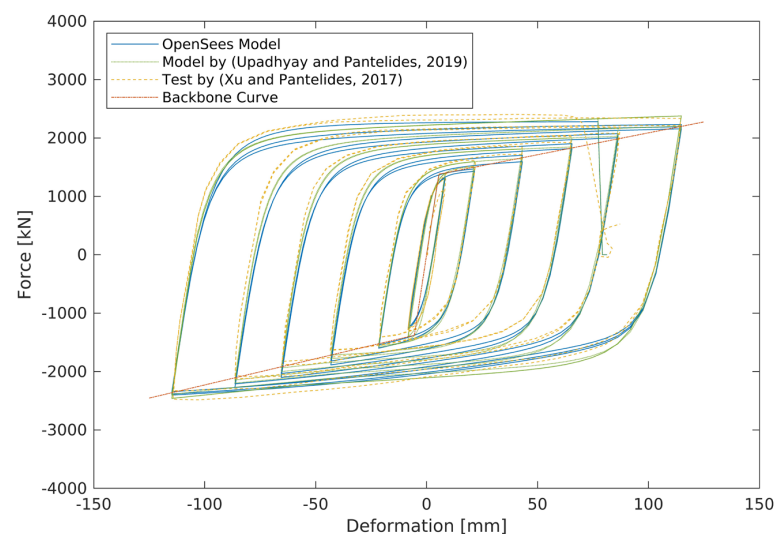
It should be noted that the use of Steel4 material allows the hysteretic behavior of the entire BRB member to be generated directly without having to model each component of the BRB using specific finite elements. Both the yielding of the steel core and the interaction between the steel core and the concrete-filled casing are implicitly accounted for when Steel4 material of OpenSees is used.

Table 3. Parameters used for Steel4 material to model BRB in the OpenSees model.

Parameters	Tension	Compression
Initial (elastic) stiffness of BRB, E_{eq}	$f_{sm}E_s$	$f_{sm}E_s$
Stiffness modification factor, f_{sm}	1.39	1.39
Elastic modulus of steel, E_s	200 GPa	200 GPa
Yield strength of BRB steel core, f_y	$\gamma_{mo}f_{ys}$	$\gamma_{mo}f_{ys}$
Material overstrength factor, γ_{mo}	1.11	1.11
Yield strength of steel, f_{ys}	248 MPa	248 MPa
Kinematic hardening ratio, b_k	0.5%	2.5%
Shape parameter *, R_0	26	26
Shape parameter *, r_1	0.91	0.89
Shape parameter *, r_2	0.10	0.02
Initial hardening ratio for isotropic materials, b_i	0.25%	0.6%
Saturated hardening ratio for isotropic materials, b_l	0.01%	0.03%
Intersection point between b_i and b_l , ρ_i	0.8	0.3
Isotropic transition parameter, R_i	3.0	3.0
Length of the yield plateau, l_{yp}	1.0	1.0
Ultimate strength of BRB steel core, f_u	$1.65 f_y$	$2.0 f_y$
Kinematic hardening to perfectly plastic transition parameter, R_u	2.0	2.0

* These are parameters to control the exponential transition from linear to kinematic hardening asymptote.

Figure 13 shows the force–displacement hysteresis loops generated using the Steel4 material with the parameters given in Table 3. The hysteresis loops obtained using OpenSees with Steel4 material are shown as solid blue lines. It can be seen that they compared well with those modeled by Upadhyay et al. [35] (shown as dotted green lines) and the experimental results obtained by Xu & Pantelides [36] (shown as dashed yellow lines).

**Figure 13.** Validation of the OpenSees model.

8. Energy-Based Design of Buckling-Restrained Braced Frames

In this section, the design of BRBs using an energy-based concept is presented. The frames equipped with these BRBs will then be analyzed using time-history analysis to show how the use of BRBs can drastically reduce frame drifts under the dual earthquake–wind excitations.

8.1. Energy Capacity of a BRB

The dashed-dotted orange lines shown in Figure 13 are the skeleton curves of the BRB. The skeleton curves representing the force–displacement relationships of two commonly used configurations of BRB are shown in Figure 14. For the chevron BRB, regardless of the direction of the applied lateral force, one BRB is under tension and the other is under

compression, and so both partake in dissipating energy. For the diagonal BRB, it is either under tension or compression depending on the direction of the lateral force (the lateral force in the figure is applied from left to right so the diagonal BRB is under tension). As a result, the amount of energy that can be dissipated is smaller. However, when the ratio of bay width to story height is small, the diagonal configuration is often used because it is more economical and easier to erect.

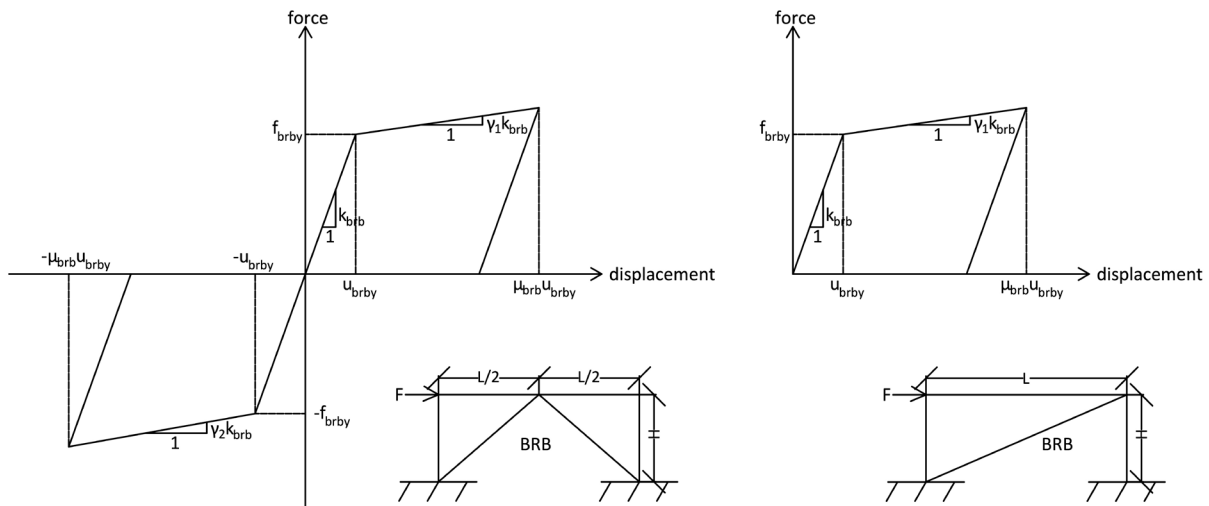


Figure 14. Force–displacement relationship of a chevron and a diagonal BRB under one cycle of loading and unloading.

The story-based capacity of the chevron BRB is computed as the sum of the strain energy and hysteretic energy, obtained as the area under the force–displacement plots, i.e.,

$$SE_i + HE_i = f_{brby} \mu_{brbi} \left[\frac{1}{2} + (\mu_{brbi} - 1) \frac{2 + \gamma_1 (\mu_{brbi} - 1)}{2} + \frac{1}{2} + (\mu_{brbi} - 1) \frac{2 + \gamma_2 (\mu_{brbi} - 1)}{2} \right] \tag{11}$$

$$= A_{brbi} \frac{\sigma_{brby}^2}{E_{brb}} L_{brbi} \left[\frac{1}{2} + (\mu_{brbi} - 1) \frac{2 + \gamma_1 (\mu_{brbi} - 1)}{2} + \frac{1}{2} + (\mu_{brbi} - 1) \frac{2 + \gamma_2 (\mu_{brbi} - 1)}{2} \right]$$

where i is the story level; SE_i and HE_i are the strain and hysteretic energies of the BRB, respectively; A_{brbi} is the cross-section area of the BRB yielding core; σ_{brby} is the material yield strength; $E_{brb} = E_{eq}$ (in Table 3) is the BRB elastic modulus; L_{brbi} is the BRB length; μ_{brbi} is the BRB ductility; and γ_1 and γ_2 are the nondimensional BRB tensile and compressive hardening ratios, determined from Figure 13 to be 0.03 and 0.036, respectively. μ_{brbi} and L_{brbi} can be calculated using the equations:

$$\mu_{brbi} = \frac{u_{brbmaxi}}{u_{brbyi}} = \frac{dr_{maxlimit} H_i}{\frac{\sigma_{brby}}{E_{brb}} L_{brbi}} \frac{\frac{L_i}{2}}{\sqrt{\left(\frac{L_i}{2}\right)^2 + H_i^2}} \tag{12}$$

$$L_{brbi} = \sqrt{\left(\frac{L_i}{2}\right)^2 + H_i^2} \tag{13}$$

where $u_{brbmaxi}$ is the target (axial) displacement of the BRB; u_{brbyi} is the yield displacement of the BRB; $dr_{maxlimit}$ is the maximum story drift ratio; and L_i and H_i are the bay width and story height, respectively.

If the chevron BRB is replaced by a diagonal BRB, the capacity becomes:

$$SE'_i + HE'_i = A_{brbi} \frac{\sigma_{brby}^2}{E_{brb}} L_{brbi} \left[\frac{1}{2} + (\mu'_{brbi} - 1) \frac{2 + \gamma_1 (\mu'_{brbi} - 1)}{2} \right] \tag{14}$$

$$\mu'_{brbi} = \frac{u_{brbmaxi}}{u_{brbyi}} = \frac{dr_{maxlimit}H_i}{\frac{\sigma_{brby}}{E_{brb}}L_{brbi}'} \frac{L_i}{\sqrt{L_i^2 + H_i^2}} \tag{15}$$

$$L_{brbi}' = \sqrt{L_i^2 + H_i^2} \tag{16}$$

where SE'_i , HE'_i , μ'_{brbi} and L_{brbi}' are the strain energy, hysteretic energy, ductility and length of the diagonal BRB, respectively. In applying Equations (11)–(16), a consistent set of units should be used. For example, if Newton (N) is used as the force unit and meter (m) is used as the length unit, the units for energy, cross-section area, material yield strength and elastic modulus will be N-m, m², N/m² and N/m², respectively.

8.2. Energy Demand from the Dual Hazards

To determine the energy demand, the idealized elastic–plastic force–displacement relationships of a typical moment frame (as shown in Figure 15) can be used. The input energy in excess of what the frame can withstand is the energy demand for the BRB. This energy demand is shown by the cross-hatched area in the figure.

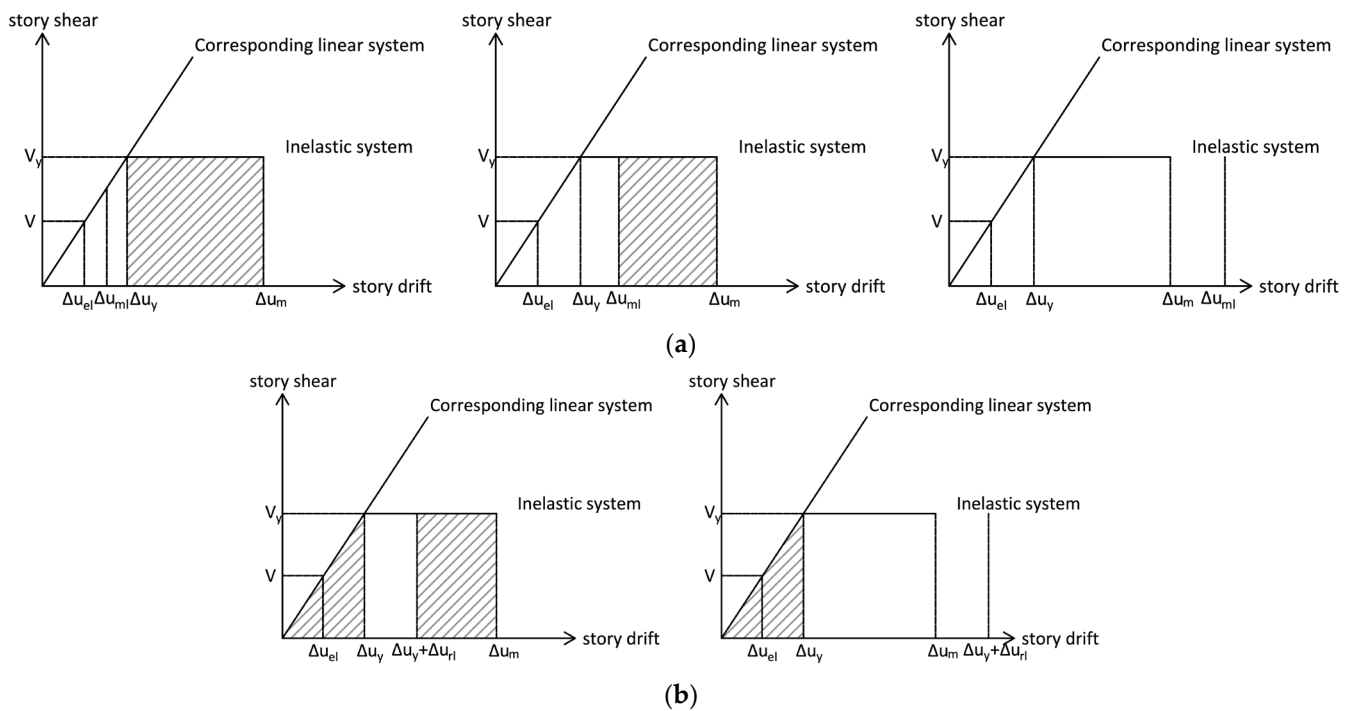


Figure 15. Force–displacement relationships of an inelastic frame and the corresponding elastic frame: (a) energy demand based on maximum drift limit, and (b) energy demand based on residual drift limit.

The energy demand (i.e., the cross-hatched areas in Figure 15) for story i can be calculated as

$$IE_i = \max\left(IE_i^{ml}, IE_i^{rl}\right) \tag{17}$$

where IE_i^{ml} and IE_i^{rl} denote the energy demand based on the maximum (peak) drift limit and residual drift limit, respectively, given by

$$IE_i^{ml} = \begin{cases} \frac{\Omega_0}{I_e} V_i \left(\Delta u_{mi} - \frac{\Delta u_{y_i}}{2} \right) - \frac{1}{2} \frac{\Omega_0}{I_e} \frac{V_i}{\Delta u_{y_i}} \Delta u_{ml}^2 & \text{if } \Delta u_{mli} < \Delta u_{y_i} \\ \frac{\Omega_0}{I_e} V_i (\Delta u_{mi} - \Delta u_{mli}) & \text{if } \Delta u_{y_i} \leq \Delta u_{mli} < \Delta u_{mi} \\ 0 & \text{if } \Delta u_{mli} \geq \Delta u_{mi} \end{cases} \tag{18}$$

$$IE_i^{rl} = \begin{cases} \frac{1}{2} \frac{\Omega_0}{I_e} V_i \Delta u_{y_i} + \frac{\Omega_0}{I_e} V_i (\Delta u_{m_i} - \Delta u_{y_i} - \Delta u_{r_i} t) & \text{if } \Delta u_{r_i} < (\Delta u_{m_i} - \Delta u_{y_i}) \\ \frac{1}{2} \frac{\Omega_0}{I_e} V_i \Delta u_{y_i} & \text{if } \Delta u_{r_i} \geq (\Delta u_{y_i} \leq \Delta u_{r_i}) \end{cases} \quad (19)$$

where Ω_0 is the nondimensional overstrength factor; $V_i = (\sum F_i)$ is the elastic story shear; F_i is the equivalent lateral force applied at story i ; I_e is the nondimensional importance factor; $\Delta u_{m_i} = \frac{C_d}{I_e} \Delta u_{e_i}$ is the inelastic inter-story drift; C_d is the nondimensional deflection amplification factor; Δu_{e_i} is the elastic inter-story drift that corresponds to V_i ; $\Delta u_{y_i} = \frac{\Delta u_{m_i}}{\mu_{frame}}$ is the inter-story drift that corresponds to yielding; $\mu_{frame} = \frac{C_d}{\Omega_0}$ is the frame ductility; $\Delta u_{m_i} = dr_{ml} H_i$ and $\Delta u_{r_i} = dr_{rl} H_i$ are the maximum (peak) and residual inter-story drifts, respectively, in which H_i is the story height; and dr_{ml} and dr_{rl} are the peak and residual inter-story drift limits. After BRBs are installed in a MRF, the frame becomes a braced frame, and with reference to Table 1, dr_{ml} is 0.5% for the performance level of IO and 1.5% for the performance level of LS, whereas dr_{rl} is negligible (i.e., near zero) for IO and 0.5% for LS.

The factors Ω_0 , C_d and I_e are dependent on the type of structure. For intermediate moment frames [37] often used in seismic design, $\Omega_0 = 3$ and $C_d = 4$; and for risk category III structures, $I_e = 1.25$. In applying Equations (17)–(19), a consistent set of units should be used. If Newtons and meters are used as the force and displacement units, respectively, then both IE_i^{ml} and IE_i^{rl} will have unit of N-m.

8.3. Proposed Energy-Based Design Procedure for BRB

Although some general guidelines for the design of BRBs are available [38], their actual design is considered proprietary by BRB manufacturers and has not been codified. However, the selection of the proper BRB for use often involves specifying the bay width and story height as well as determining the cross-section area of the yielding core of the BRB. The design procedure proposed herein uses the energy-balanced approach and calculates the required cross-section area of the BRB yielding core by equating its energy dissipation capacity with the energy demand from the dual excitations. The proposed energy-based BRB design procedure uses the equivalent lateral force approach [1,16] and is outlined as follows:

Step 1: Construct elastic response spectra for the dual excitations. Pseudo (or spectral) acceleration response spectra (often expressed in m/s^2 or in terms of acceleration due to gravity, g) are plots of pseudo accelerations S_a against system periods T (in seconds). These spectra can be constructed for the dual excitations using software such as Bispec, SeismoSoft, OpenSees, etc.

Step 2: Run a modal analysis to obtain (or estimate) the fundamental period for the intermediate moment frame.

Step 3: Calculate the base shear using the equation

$$V_b = \sum_i^n C_{s_i} w_i \quad (20)$$

where w_i is the seismic mass of story i , and C_{s_i} is the response coefficient of story i given by

$$C_{s_i} = \frac{S_{a_i}}{R I_e} \quad (21)$$

in which S_{a_i} is the spectral acceleration response of the dual earthquake–wind excitations at story i evaluated at the fundamental period T ; R is the nondimensional response modification factor (=4.5 for intermediate moment frames); and I_e is the nondimensional importance factor (=1.25 for risk category III structures).

Step 4: Determine the equivalent lateral force (ELF) and story shear at story i using the equation:

$$F_i = C_{vi} V_b \quad (22)$$

where C_{vi} is the nondimensional base shear distribution factor computed from the equation:

$$C_{vi} = \frac{C_{si} w_i h_i^k}{\sum_i^n C_{si} w_i h_i^k} \quad (23)$$

in which h_i is the height from the base of the building to floor i , and k is an exponent related to the structure period T . For T less than or equal to 0.5 s, k is 1. For T greater than or equal to 2.5 s, k is 2. For T between 0.5 s and 2.5 s, k is equal to $0.5T + 0.75$.

The story shear force at the i -th floor V_i can be calculated from the equation:

$$V_i = \sum_i^n F_i \quad (24)$$

Step 5: Perform a linear static analysis on the intermediate moment resisting frame subject to this ELF and determine its maximum inter-story displacement response Δu_{el} . The maximum displacement response of the frame accounting for inelasticity Δu_m can be estimated using the equation:

$$\Delta u_m = \frac{C_d}{I_e} \Delta u_{el} \quad (25)$$

where C_d is the nondimensional deflection amplification factor (= 4 for intermediate moment frames) and $I_e = 1.25$ is the nondimensional importance factor for risk category III structures.

Step 6: Use the energy equation to determine the required BRB cross-section area for each story. The required BRB yielding core area can be obtained by equating Equation (11) or Equation (14) with Equation (17) and solving for A_{brbi} to give

$$A_{brbi} = \frac{SE_i + HE_i}{\eta_i} = \frac{IE_i}{\eta_i} \quad (26)$$

where for a chevron BRB, η_i is given by

$$\eta_i = \frac{\sigma_{brby}^2}{E_{brb}} L_{brbi} \left[\frac{1}{2} + (\mu_{brbi} - 1) \frac{2 + \gamma_1(\mu_{brbi} - 1)}{2} + \frac{1}{2} + (\mu_{brbi} - 1) \frac{2 + \gamma_2(\mu_{brbi} - 1)}{2} \right] \quad (27)$$

and for a diagonal BRB, η'_i is given by

$$\eta'_i = \frac{\sigma_{brby}^2}{E_{brb}} L_{brbi} \left[\frac{1}{2} + (\mu'_{brbi} - 1) \frac{2 + \gamma_1(\mu'_{brbi} - 1)}{2} \right] \quad (28)$$

As before, a consistent set of units (e.g., N for force and m for length) should be used in applying Equations (20)–(28).

9. Analysis Results for Buckling-Restrained-Braced-Frame Responses to Dual Earthquake and Wind Hazards

The multi-story moment frames analyzed in Section 6 for the dual hazards do not always satisfy the FEMA 356 [11] seismic-performance-based design drift criteria given in Table 1. In this section, chevron BRBs are designed for these frames so their peak and residual inter-story drift ratios will fall within or near the FEMA 356 [11] recommended limits. Chevron BRBs are used because of their higher energy-dissipation efficiency and because of the relatively large bay width to story height ratios for these frames. The design details for the required BRB's yielding core cross-section area for each story of these two frames are given in Tables A3–A10 in Appendix A. These cross-section sizes were selected based on the availability of BRBs from manufacturers such as the Seismic Bracing Company (<https://www.thesbcllc.com>) (accessed on 1 September 2023). The design is based on both

IO and LS to ensure that the final design will satisfy both performance levels in accordance with performance-based seismic design for category III structures.

9.1. Three-Story Frame

For simplicity and to maintain a certain level of uniformity, only one BRB size was selected for use in the three-story frame, although the computed BRB sizes vary from story to story. This one size was obtained by taking the average of the cross-section areas of the BRB yielding steel core computed for each of the three stories. The final designs and arrangements of BRBs for the three-story BRBFs in Los Angeles and Charleston, for the performance levels of IO and LS, are summarized in Table 4 and Figure 16. For Los Angeles, the calculated BRB area was relatively large and so more BRBs needed to be used. To accommodate these BRBs, they need to be placed in two bays. As for Charleston, the required BRB area was small enough that placement of these BRBs in just one bay was adequate.

Table 4. Final design of the three-story BRBF.

Model	$A_{brb}[\text{cm}^2]$	Configuration
Los Angeles for IO	387	2-bay
Los Angeles for LS	206	2-bay
Charleston for IO	206	1-bay
Charleston for LS	71	1-bay

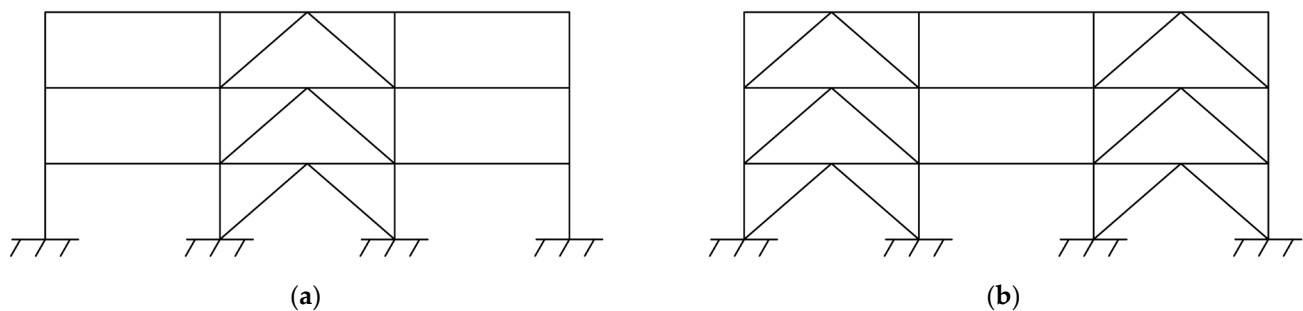


Figure 16. Placement of BRBs for the three-story BRBF: (a) one-bay BRBF and (b) two-bay BRBF.

The analysis results for the peak and residual inter-story and roof drift ratios of the three-story BRBF are shown in Figure 17. The solid magenta lines represent results obtained for the BRBF designed for IO while the dashed black lines depict the results for the LS design. It can be seen that both the inter-story and roof drift ratios of the BRBF in Los Angeles decrease noticeably from those of the MRF, so much so that the frame now satisfies the FEMA 356 recommended deflection criteria for both the performance levels of IO and LS. The mean peak inter-story and roof drift ratios of the BRBF designed for IO are now 0.27% and 0.27%, and for LS they are 0.80% and 0.52%, respectively. The mean residual inter-story and residual roof drift ratios for IO are both very small ($\approx 0.01\%$), indicating that the frame behaves more or less elastically with no permanent deformations after the dual hazards. As for performance level of LS, the residual inter-story and residual roof drift ratios are 0.14% and 0.06%, respectively, which are also quite small.

The peak and residual inter-story and roof drift responses of the BRBF in Charleston are shown in Figure 18. The addition of BRBs helps reduce drifts in the design for LS, especially in the top story. This is because the BRB used for the frame was based on the average of the required BRB bracing core areas computed for all three stories, and the required BRB area for the top story was smaller than this average value. It can be seen that the mean peak and residual inter-story drift ratios of the BRBF were 0.27% and negligible ($\approx 0\%$) for the performance level of IO, and 0.86% and 0.2% for the performance level of LS; meanwhile, the mean peak and residual roof drift ratios were 0.25% and $\approx 0\%$ for IO, and 0.66% and 0.14% for LS.

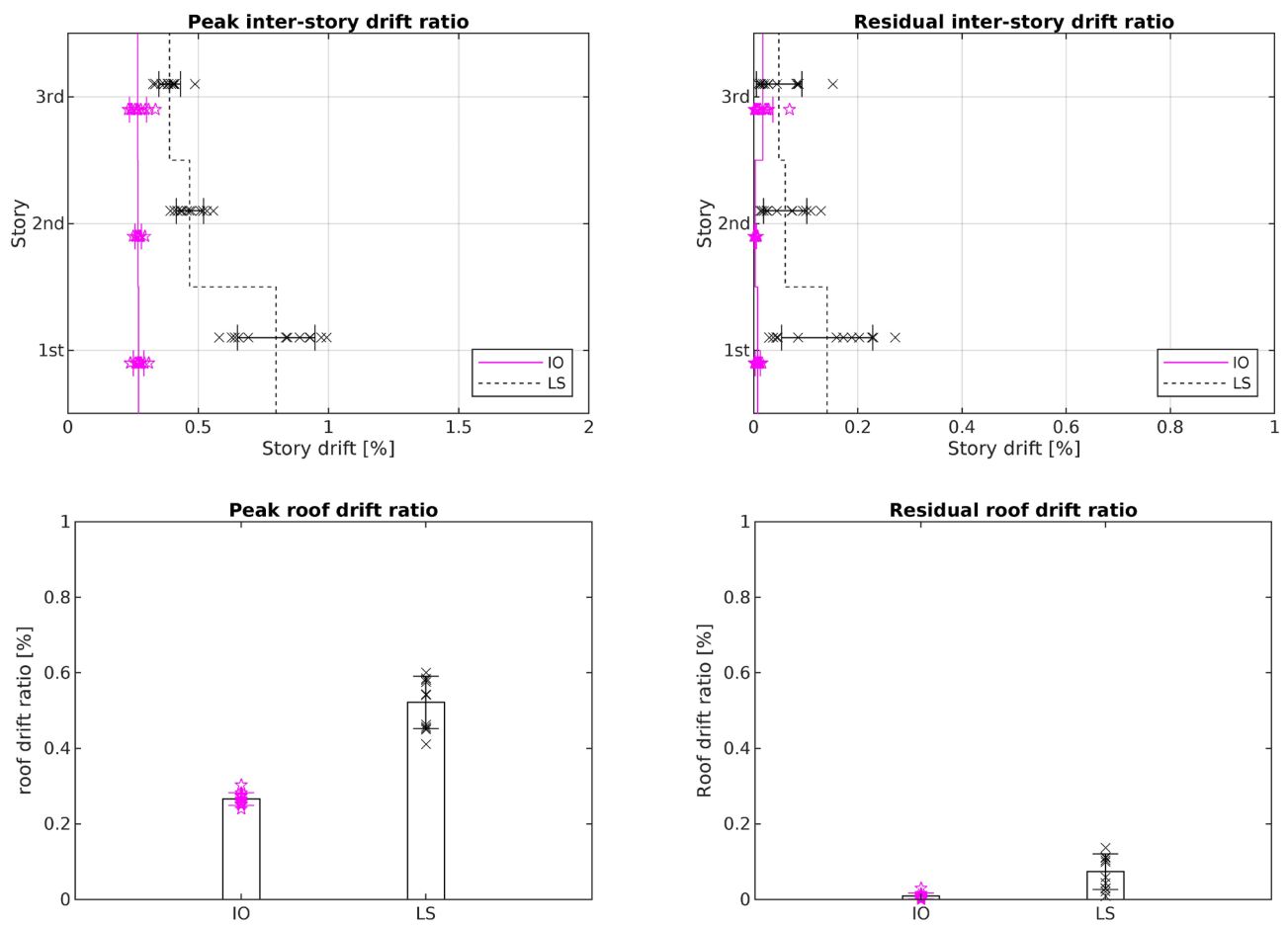


Figure 17. Peak and residual inter-story and roof drift ratios of the three-story BRBF in Los Angeles.

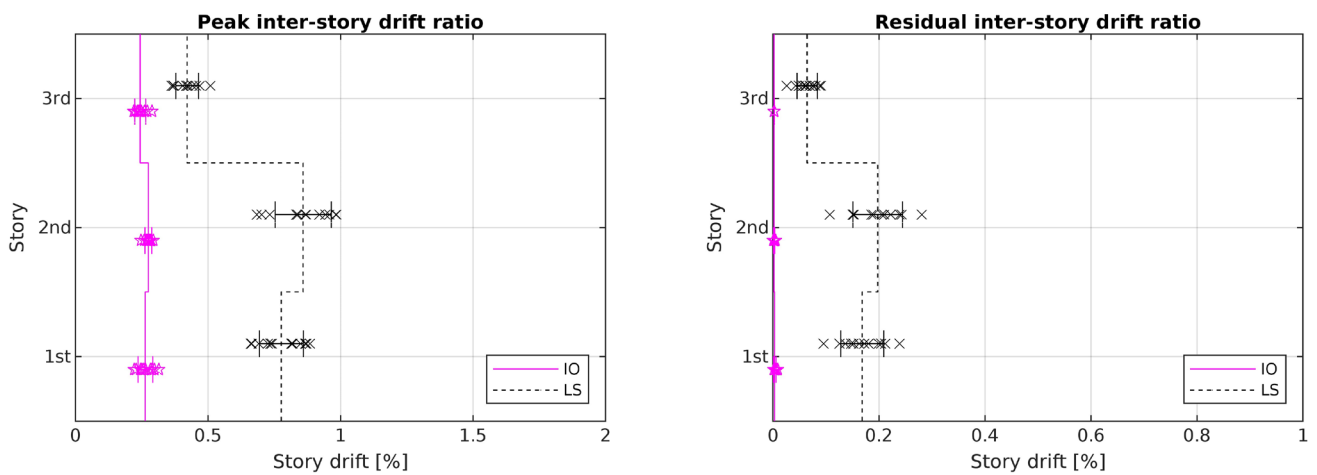


Figure 18. Cont.

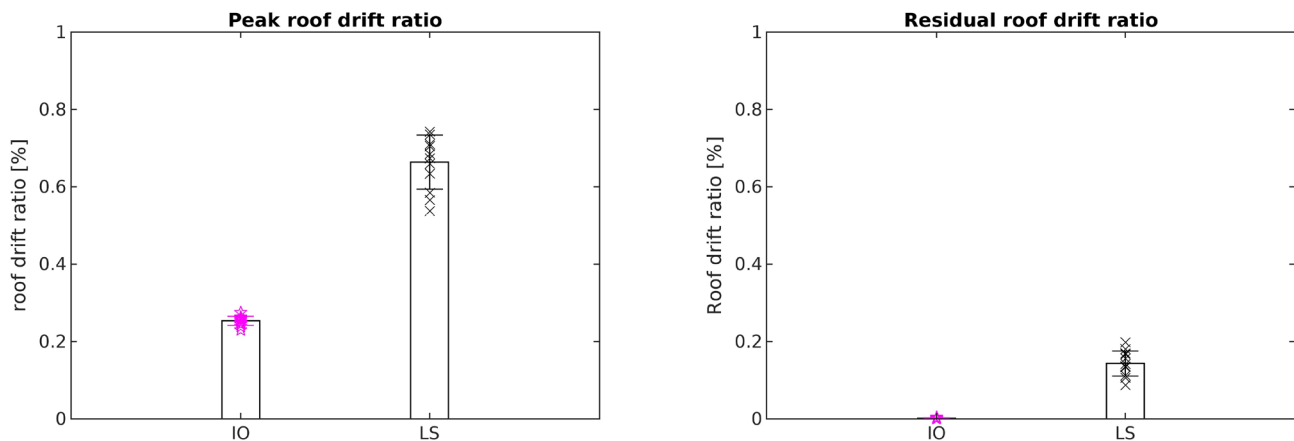


Figure 18. Peak and residual inter-story and roof drift ratios of the three-story BRBF in Charleston.

The proposed BRB design method results in a relatively conservative design for the three-story BRBF. The selected BRB was larger than what was required for the top story, and so the drift ratios of this story were noticeably decreased, especially at the LS performance level when larger drift limits were allowed.

9.2. Nine-Story Frame

For the nine-story frame, four different sizes of BRBs were used. The analysis showed that the top and bottom stories required the smallest and largest BRB cross-section areas, respectively, so each was accorded a specific BRB size. The BRB sizes computed for the second to fifth floors did not vary appreciably and so one BRB size—obtained by taking the average of these BRB areas—was used. Similarly, a single BRB size for the sixth to eighth stories was selected based on the average of the required BRB areas for these stories. The final designs and placements of BRBs for the nine-story BRBF in Los Angeles and Charleston for the performance levels of IO and LS are summarized in Table 5 and Figure 19. Depending on the required BRB sizes, their placement in a symmetric pattern from two to four bays of the frame (as shown in Figure 16) is recommended.

Table 5. Final design of the nine-story BRBF.

Model	A_{brb} [cm ²]				Configuration
	1st	2nd–5th	6th–8th	9th	
Los Angeles for IO	84	219	310	361	4-bay
Los Angeles for LS	65	181	232	284	3-bay
Charleston for IO	42	168	245	310	3-bay
Charleston for LS	21	90	123	155	2-bay

Time-history analysis results for the nine-story frame in LA are given in Figure 20. It can be seen that the mean peak inter-story and roof drift ratios of 0.64% and 0.56% for the BRBF designed for IO are somewhat larger than the FEMA-recommended drift limit of 0.5%. On the other hand, the frame designed for LS, which was shown earlier to not be able to survive the combined actions of the earthquake and wind hazards, is now able to withstand the dual excitations with the addition of BRBs. The mean peak inter-story and roof drift ratios are 1.33% and 0.80%, and the mean residual inter-story and roof drift ratios are 0.5% and 0.21%, respectively. Therefore, they all satisfy the FEMA-recommended drift limits for LS.

For the nine-story BRBF located in Charleston, it can be seen from Figure 21 that the mean peak inter-story drift ratios are 0.30% for the IO design and 1.41% for the LS design. However, for the bottom three stories, their mean residual inter-story drift ratios for the LS design exceed the FEMA-recommended drift limit of 0.5%. Note that the drift ratio computed for one of the 12 ground motions is much larger than the others. This causes the mean story drift to increase. As for the mean peak and residual roof drift ratios, their values are 0.26% and $\approx 0\%$ for IO, and 0.89% and 0.33% for LS, respectively. These all fall below the FEMA-recommended drift limits for the design under the performance levels of IO and LS.

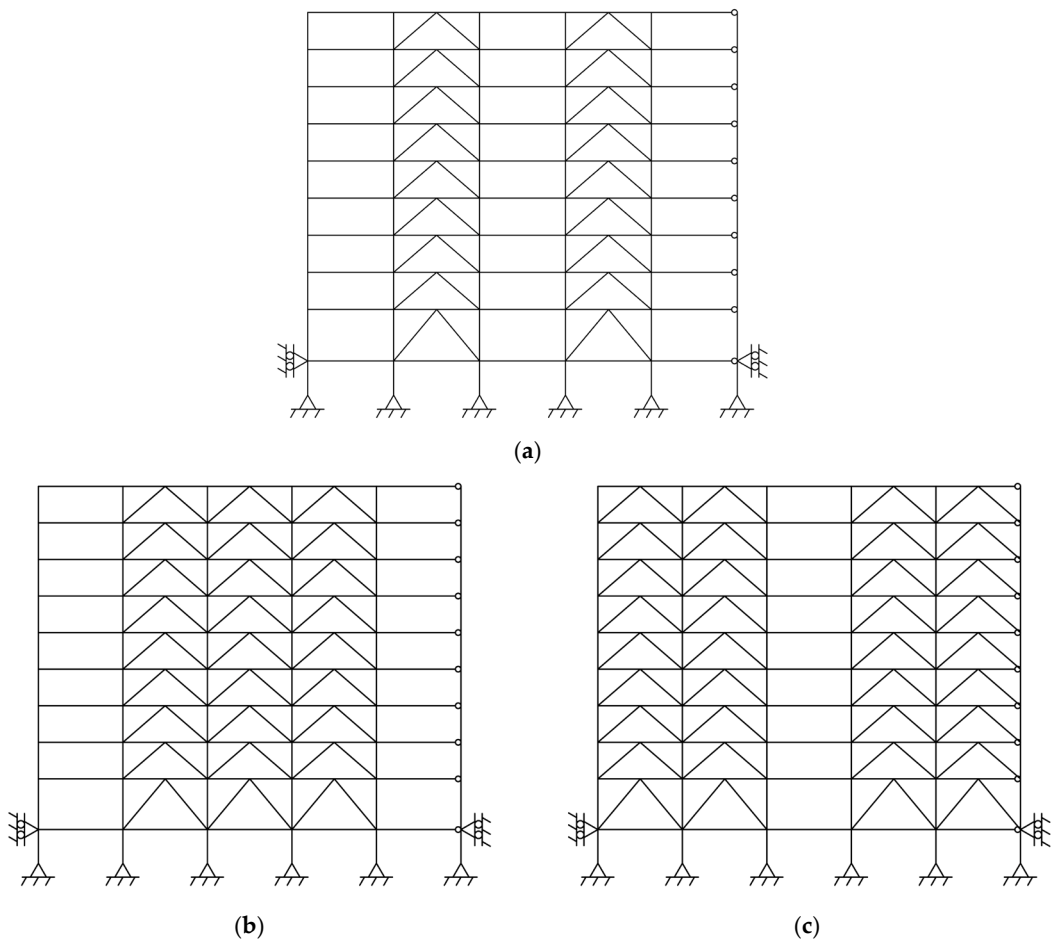


Figure 19. Placement of BRBs for the nine-story BRBF: (a) two-bay BRBF, (b) three-bay BRBF and (c) four-bay BRBF.

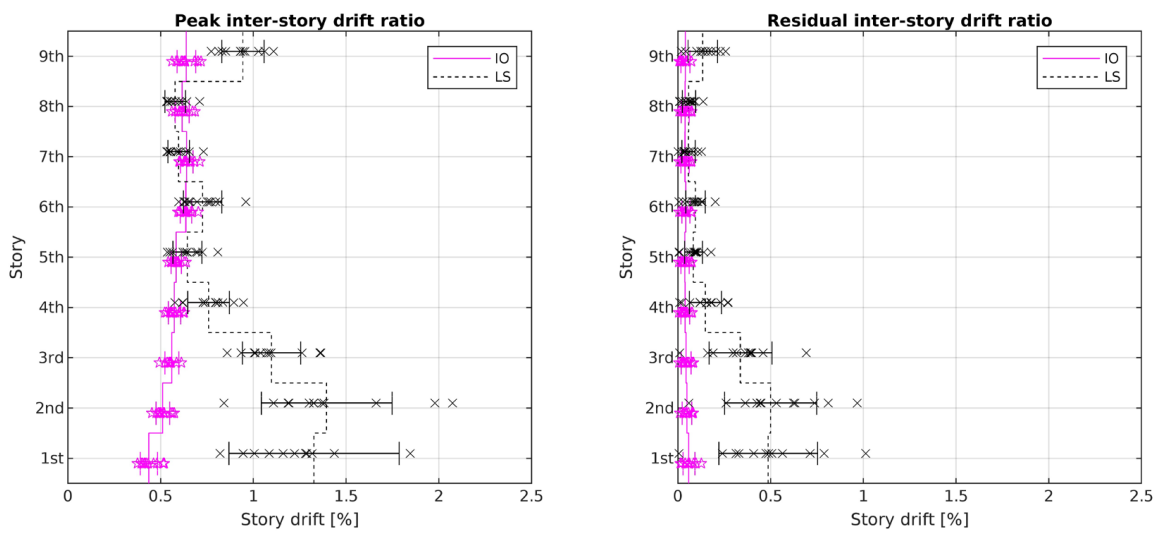


Figure 20. Cont.

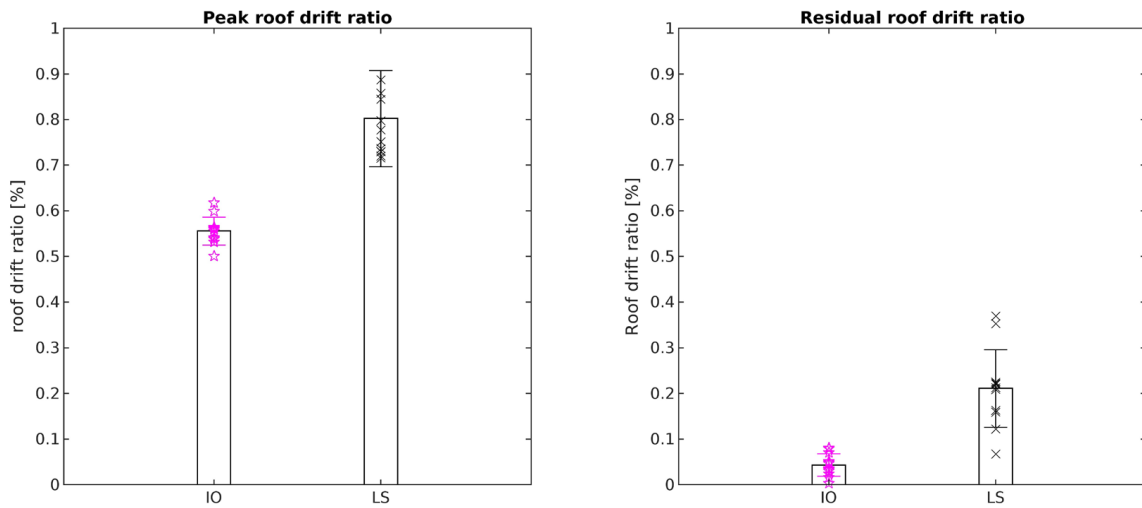


Figure 20. Peak and residual inter-story and roof drift ratios of the nine-story BRBF in Los Angeles.

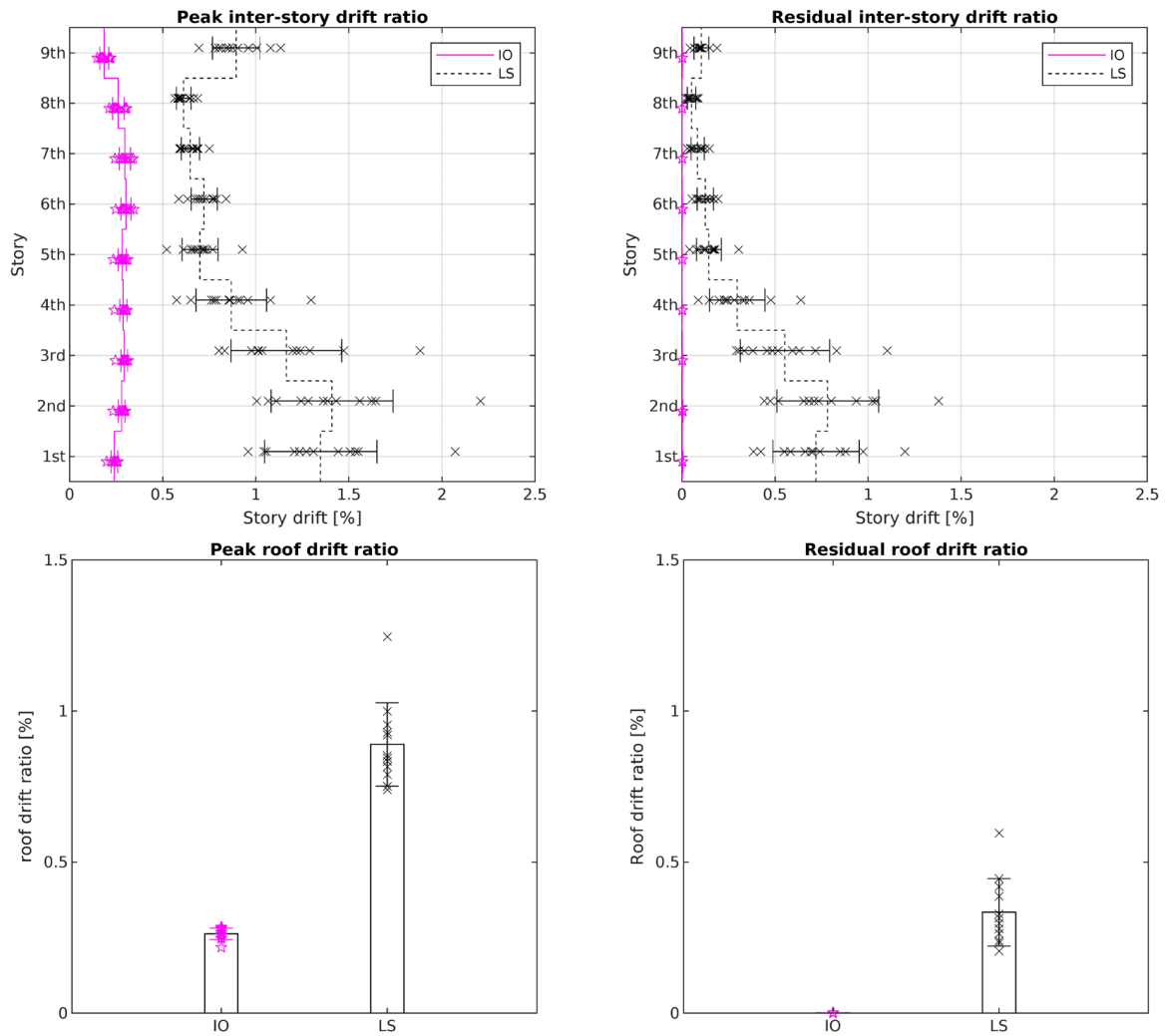


Figure 21. Peak and residual inter-story roof drift ratios of the nine-story BRBF in Charleston.

10. Results and Discussion

The analysis results presented earlier in Figures 5, 6, 8, 9, 17 and 18 for the three-story moment resisting frame (MRF) and buckling-restrained braced frame (BRBF) and in Figures 11, 20 and 21 for the nine-story MRF and BRBF are summarized in Tables 6–9.

Table 6. Comparison of drift ratios for single and dual hazards for the three-story frame without BRBs.

City	Performance Level	Hazard	Peak Inter-Story	Residual Inter-Story	Peak Roof	Residual Roof
Los Angeles	IO	Earthquake	3.25%	1.06%	2.47%	0.92%
		Wind	0.36%	≈0%	0.31%	≈0%
		Dual	4.10%	2.24%	3.46%	2.08%
	LS	Earthquake	6.80%	4.52%	5.94%	4.32%
		Wind	0.47%	≈0%	0.40%	≈0%
		Dual	11.63%	10.40%	10.99%	10.08%
Charleston	IO	Earthquake	1.14%	0.083%	0.96%	0.06%
		Wind	0.93%	0.11%	0.78%	0.09%
		Dual	1.93%	0.93%	1.65%	0.75%
	LS	Earthquake	1.75%	0.32%	1.39%	0.24%
		Wind	1.35%	0.42%	1.14%	0.36%
		Dual	3.57%	2.62%	3.27%	2.42%

Table 7. Comparison of drift ratios for single and dual hazards for the nine-story frame without BRBs.

City	Performance Level	Hazard	Peak Inter-Story	Residual Inter-Story	Peak Roof	Residual Roof
Los Angeles	IO	Earthquake	2.52%	1.00%	1.82%	0.74%
		Wind	0.77%	≈0%	0.61%	≈0%
		Dual	10.4%	9.83%	6.72%	6.19%
	LS	Earthquake	4.36%	2.83%	3.20%	2.19%
		Wind	1.08%	0.35%	0.78%	0.14%
		Dual	C *	C *	C *	C *
Charleston	IO	Earthquake	1.30%	0.16%	0.84%	0.08%
		Wind	9.40%	8.70%	4.92%	4.38%
		Dual	C *	C *	C *	C *
	LS	Earthquake	1.71%	0.41%	1.18%	0.26%
		Wind	C *	C *	C *	C *
		Dual	C *	C *	C *	C *

* The letter C denotes convergence problems due to excessive frame deflections.

Table 8. Comparison of drift ratios before and after the addition of BRBs for the three-story frame.

City	Performance Level	Frame Type	Peak Inter-Story	Residual Inter-Story	Peak Roof	Residual Roof
Los Angeles	IO	MRF	4.10%	2.24%	3.46%	2.08%
		BRBF	0.27%	0.01%	0.27%	0.01%
	LS	MRF	11.65%	10.40%	10.99%	10.08%
		BRBF	0.80%	0.14%	0.52%	0.06%
Charleston	IO	MRF	1.93%	0.93%	1.65%	0.75%
		BRBF	0.27%	≈0%	0.25%	≈0%
	LS	MRF	3.57%	2.62%	3.27%	2.42%
		BRBF	0.86%	0.20%	0.66%	0.14%

Table 9. Comparison of drift ratios before and after the addition of BRBs for the nine-story frame.

City	Performance Level	Frame Type	Peak Inter-Story	Residual Inter-Story	Peak Roof	Residual Roof
Los Angeles	IO	MRF	10.40%	9.83%	6.72%	6.19%
		BRBF	0.64%	0.05%	0.56%	0.05%
	LS	MRF	C *	C *	C *	C *
		BRBF	1.33%	0.50%	0.80%	0.21%
Charleston	IO	MRF	C *	C *	C *	C *
		BRBF	0.30%	≈0%	0.26%	≈0%
	LS	MRF	C *	C *	C *	C *
		BRBF	1.41%	0.76%	0.89%	0.33%

* The letter C denotes convergence problems due to excessive frame deflections.

In Table 6, the analysis results for the mean peak and residual inter-story and roof drift ratios of the three-story steel frame located in Los Angeles and Charleston under the performance levels of IO and LS are presented. The corresponding analysis results for the nine-story frame are given in Table 7. As can be seen, the drift ratios due to the dual earthquake–wind hazards for the nine-story frame are noticeably higher than those for the three-story frame because wind load increases as the height of a building increases. For cases that are marked with the letter C, frame deflections were so large that convergence became a problem, signifying incipient failure of the frame. Furthermore, it can be seen that the dynamic responses of the frames subjected to dual excitations cannot be obtained by summing their respective dynamic responses due to earthquakes and wind excitations only. This is because when one of the hazards causes inelasticity to occur in the frame, the effect will be exacerbated when both hazards occur concurrently (as depicted in Figures 10 and 12).

In Tables 8 and 9, the analysis results for the mean peak and residual inter-story and roof drift ratios of the three-story and nine-story steel frames in Los Angeles and Charleston under the performance levels of IO and LS are compared for the MRF and BRBF, i.e., before and after the addition of BRBs. As can be seen, a noticeable decrease in drifts is observed after the addition of BRBs. In particular, the nine-story frame that experiences excessive deformations (large enough to cause collapse without the BRBs) is able to withstand the dual hazards after BRBs are installed.

It should be noted that the present study is focused only on the serviceability (IO) and safety (LS) aspects of these frames when subject to the dual earthquake–wind hazards. Material, fabrication and installation costs of the BRBs are not considered since cost analysis is not part of the present study. It is, however, perceivable that the BRBF frames will cost more and the construction times for these frames will be longer.

11. Summary and Conclusions

Traditionally, engineers design buildings with a focus on just a single hazard—earthquake or wind—based on the geographic location and the building’s risk category. However, designing structures for one dominant hazard without considering the other could result in an unsafe design, especially when both hazards happen to occur concurrently. Designers interested in investigating the effect of both earthquakes and wind on structural behavior often resort to performing the analyses and designs for earthquake and for wind separately. Moreover, the design for wind often treats wind as a static load when its effect is dynamic in nature.

In the present study, a dual hazard spectrum that allows engineers to consider both the static effect of wind as well as the dynamic effects of earthquakes and wind is proposed. This dual earthquake–wind power spectrum is obtained by combining the earthquake and wind power spectral densities using the SRSS combination rule as shown in Equation (8). Using this dual hazard spectrum, time-varying dual hazard excitations can then be generated using Equation (9) and used to determine whether the design is adequate under the effect of dual excitations.

For buildings that do not satisfy the drift requirements, buckling restrained braces (BRBs) are added as supplementary energy-dissipation devices. An energy-based procedure using the well-known equivalent lateral force approach in seismic design is proposed for the design of these BRBs. When applied to two multistory frames, it was shown that the proposed procedure successfully reduced the peak and residual inter-story and roof drift ratios to below or near the FEMA 356 [11] recommended drift limits.

Based on the results of the present study, the following conclusions can be made.

1. When compared to results obtained for earthquake only or wind only excitation, the two steel frames used in the present study were shown to experience peak and residual inter-story and roof drift ratios that were noticeably higher under the dual earthquake–wind excitations.
2. From Tables 6 and 7, it can be seen that dynamic responses due to the combined earthquake–wind dual excitations cannot be obtained just by adding the dynamic responses due to earthquake only and wind only excitations. This is because of the presence of inelasticity. Once the structure experiences yielding, inelastic deformations will increase rapidly with the applied forces (as illustrated in Figures 10 and 12).
3. By retrofitting these frames with BRBs using the proposed energy-based design methodology presented in Section 8, the drift ratios of these frames were drastically reduced, and they all fell below or came very close to the FEMA 356 drift limits.

Author Contributions: Conceptualization, E.M.L.; methodology, T.S. and E.M.L.; validation, T.S. and E.M.L.; formal analysis, T.S.; investigation: T.S.; resources, E.M.L.; data curation, T.S.; writing—original draft, T.S.; writing—review and editing, E.M.L.; visualization, T.S.; supervision, E.M.L.; project administration, E.M.L. All authors have read and agreed to the published version of the manuscript.

Funding: This research received no external funding.

Data Availability Statement: All data generated and analyzed during this study are included in this published article.

Acknowledgments: Funding, in the form of a research fellowship provided by the Graduate School of Syracuse University to the first author, is deeply appreciated.

Conflicts of Interest: Taonian Shan is an employee of Creighton Manning Engineering. The authors declare no conflicts of interest.

List of Abbreviations

ASCE	American Society of Civil Engineers
BRB	Buckling Restrained Brace
BRBF	Buckling-Restrained-Braced Frame
DBE	Design Based Earthquakes
EDP	Engineering Demand Parameters
ELF	Equivalent Lateral Force
FEMA	Federal Emergency Management Agency
FFT	Fast Fourier Transform
IBC	International Building Code
IFFT	Inverse Fast Fourier Transform
IO	Immediate Occupancy
LS	Life Safety
MCE	Maximum Considered Earthquakes
MRF	Moment Resisting Frame
PSD	Power Spectral Density
RSN	Record Sequence Number
SEI	Structural Engineering Institute
SRSS	Square Root of the Sum of Squares

Appendix A

Table A1. Selected ground motion records for site class CD.

RSN	Event	Year	Station Name	Magnitude	V _{s30} (m/s)
100	“Hollister-03”	1974	“San Juan Bautista_ 24 Polk St”	5.14	336
187	“Imperial Valley-06”	1979	“Parachute Test Site”	6.53	347
280	“Trinidad”	1980	“Rio Dell Overpass-FF”	7.2	312

Table A1. *Cont.*

RSN	Event	Year	Station Name	Magnitude	Vs ₃₀ (m/s)
292	"Irpinia_ Italy-01"	1980	"Sturno (STN)"	6.9	382
313	"Corinth_ Greece"	1981	"Corinth"	6.6	361
725	"Superstition Hills-02"	1987	"Poe Road (temp)"	6.54	317
832	"Landers"	1992	"Amboy"	7.28	383
1119	"Kobe_ Japan"	1995	"Takarazuka"	6.9	312
1762	"Hector Mine"	1999	"Amboy"	7.13	383
2093	"Nenana Mountain_ Alaska"	2002	"TAPS Pump Station #09"	6.7	383
5865	"El Mayor-Cucapah_ Mexico"	2010	"Palm Springs Airport"	7.2	312
6911	"Darfield_ New Zealand"	2010	"HORC"	7	326

Table A2. Selected ground motion records for site class DE.

RSN	Event	Year	Station Name	Magnitude	Vs ₃₀ (m/s)
26	"Hollister-01"	1961	"Hollister City Hall"	5.6	198.8
35	"Northern Calif-06"	1967	"Hollister City Hall"	5.2	198.8
163	"Imperial Valley-06"	1979	"Calipatria Fire Station"	6.53	206
314	"Westmorland"	1981	"Brawley Airport"	5.9	209
462	"Morgan Hill"	1984	"Hollister City Hall"	6.19	198.8
718	"Superstition Hills-01"	1987	"Imperial Valley Wildlife"	6.22	179.0
1931	"Anza-02"	2001	"El Centro Array #10"	4.92	203
1992	"Gulf of California"	2001	"Calipatria Fire Station"	5.7	206
4100	"Parkfield-02_ CA"	2004	"Parkfield-Cholame 2WA"	6	173.0
4462	"L'Aquila_ Italy"	2009	"Avezzano"	6.3	199.0
180	"Imperial Valley-06"	1979	"El Centro Array #5"	6.53	206
726	"Superstition Hills-02"	1987	"Salton Sea Wildlife Refuge"	6.54	191.1

Table A3. BRB design of the three-story frame in Los Angeles for IO.

Story	S _a [g]	C _s	W[kN]	W _{eff} [kN]	C _v	F _i [kN]	IE _i [kN·m]	A _{brbi} ^r [cm ²]
3	0.941	0.261	5101	5075	0.557	2121	416	616
2	0.952	0.264	4694	4724	0.312	1189	647	960
1	0.946	0.263	4694	4694	0.1305	497	505	750

Table A4. BRB design of the three-story frame in Los Angeles for LS.

Story	S _a [g]	C _s	W[kN]	W _{eff} [kN]	C _v	F _i [kN]	IE _i [kN·m]	A _{brbi} ^r [cm ²]
3	1.422	0.395	5101	5089	0.558	3205	857	337
2	1.435	0.398	4694	4723	0.312	1792	1331	523
1	1.426	0.396	4694	4694	0.1303	749	908	357

Table A5. BRB design of the three-story frame in Charleston for IO.

Story	S _a [g]	C _s	W[kN]	W _{eff} [kN]	C _v	F _i [kN]	IE _i [kN·m]	A _{brbi} ^r [cm ²]
3	0.435	0.1207	5101	4223	0.513	1017	96.7	143
2	0.523	0.1453	4694	4678	0.342	679	169.1	251
1	0.525	0.1458	4694	4694	0.1445	286	136.8	203

Table A6. BRB design of the three-story frame in Charleston for LS.

Story	S _a [g]	C _s	W[kN]	W _{eff} [kN]	C _v	F _i [kN]	IE _i [kN·m]	A _{brbi} ^r [cm ²]
3	0.625	0.1735	5101	4380	0.521	1452	127.5	50
2	0.732	0.2033	4694	4722	0.338	943	223	88
1	0.728	0.2021	4694	4694	0.1413	394	162.5	64

Table A7. BRB design of the nine-story frame in Los Angeles for IO.

Story	S_a [g]	C_s	W[kN]	W_{eff} [kN]	C_v	F_i [kN]	IE_i [kN·m]	A_{brbi}^r [cm ²]
9	0.433	0.1202	5248	5247	0.273	1482	222	330
8	0.456	0.1265	4856	5108	0.215	1168	502	744
7	0.453	0.1257	4856	5077	0.1681	914	621	921
6	0.450	0.1249	4856	5043	0.1271	691	631	936
5	0.446	0.1240	4856	5007	0.0916	498	763	1131
4	0.443	0.1231	4856	4968	0.0618	336	792	1174
3	0.439	0.1220	4856	4924	0.0376	205	801	1187
2	0.435	0.1208	4856	4875	0.01930	104.9	770	1143
1	0.433	0.1203	4954	4954	0.00707	38.4	1138	1440

Table A8. BRB design of the nine-story frame in Los Angeles for LS.

Story	S_a [g]	C_s	W[kN]	W_{eff} [kN]	C_v	F_i [kN]	IE_i [kN·m]	A_{brbi}^r [cm ²]
9	0.690	0.1918	5248	5245	0.275	2368	483	190
8	0.717	0.1991	4856	5039	0.213	1840	1146	450
7	0.714	0.1982	4856	5016	0.1674	1443	1387	545
6	0.710	0.1973	4856	4993	0.1267	1093	1342	527
5	0.707	0.1963	4856	4967	0.0915	789	1665	654
4	0.703	0.1952	4856	4939	0.0619	533	1712	672
3	0.698	0.1939	4856	4907	0.0378	326	1716	674
2	0.693	0.1925	4856	4871	0.01943	167.5	1617	635
1	0.691	0.1919	4954	4954	0.00712	61.4	2437	816

Table A9. BRB design of the nine-story frame in Charleston for IO.

Story	S_a [g]	C_s	W[kN]	W_{eff} [kN]	C_v	F_i [kN]	IE_i [kN·m]	A_{brbi}^r [cm ²]
9	0.252	0.0699	5248	3879	0.205	875	81.1	120
8	0.403	0.1119	4856	5744	0.245	1049	262	389
7	0.392	0.1088	4856	5583	0.1879	803	362	537
6	0.380	0.1054	4856	5411	0.1385	592	384	569
5	0.366	0.1018	4856	5224	0.0971	415	470	698
4	0.352	0.0978	4856	5019	0.0634	271	490	727
3	0.336	0.0934	4856	4794	0.0372	159.1	495	734
2	0.319	0.0886	4856	4546	0.01829	78.1	475	705
1	0.341	0.0946	4954	4954	0.00718	30.7	702	889

Table A10. BRB design of the nine-story frame in Charleston for LS.

Story	S_a [g]	C_s	W[kN]	W_{eff} [kN]	C_v	F_i [kN]	IE_i [kN·m]	A_{brbi}^r [cm ²]
9	0.354	0.0984	5248	4022	0.214	1233	100.9	40
8	0.531	0.1474	4856	5576	0.240	1382	366	144
7	0.518	0.1440	4856	5447	0.1849	1064	485	191
6	0.505	0.1403	4856	5307	0.1370	788	483	190
5	0.490	0.1362	4856	5155	0.0966	556	613	241
4	0.474	0.1318	4856	4987	0.0635	366	631	248
3	0.456	0.1268	4856	4798	0.0376	216	631	248
2	0.436	0.1212	4856	4585	0.01860	107.0	591	232
1	0.462	0.1283	4954	4954	0.00724	41.7	895	300

References

1. ASCE/SEI 7-22; Minimum Design Loads and Associated Criteria for Buildings and Other Structures. American Society of Civil Engineers: Reston, VA, USA, 2022. Available online: <https://ascelibrary.org/doi/book/10.1061/9780784415788> (accessed on 1 July 2023).
2. Fan, W.; McGuire, J.J.; de Groot-Hedlin, C.D.; Hedlin, M.A.H.; Coats, S.; Fiedler, J.W. Stormquakes. *Geophys. Res. Lett.* **2019**, *46*, 12909–12918. [CrossRef]

3. Duthinh, D.; Simiu, E. Safety of structures in strong winds and earthquakes: Multihazard considerations. *J. Struct. Eng.* **2010**, *136*, 330–333. [CrossRef]
4. Crosti, C.; Duthinh, D.; Simiu, E. Risk consistency and synergy in multihazard design. *J. Struct. Eng.* **2011**, *137*, 844–849. [CrossRef]
5. Aly, A.M. Design of buildings for wind and earthquake. In Proceedings of the 2014 World Congress on Advances in Civil, Environmental, and Materials Research, ACEM14, Busan, Republic of Korea, 24–28 August 2014.
6. Aly, A.M.; Abburu, S. On the design of high-rise buildings for multihazard: Fundamental differences between wind and earthquake demand. *Shock. Vib.* **2015**, *2015*, 148681. [CrossRef]
7. Thilakarathna, S.N.; Anwar, N.; Norachan, P.; Naja, F.A. The effect of wind loads on the seismic performance of tall buildings. *Athens J. Technol. Eng.* **2018**, *5*, 251–276. [CrossRef]
8. Mazza, F.; Vulcano, A. Control of the earthquake and wind dynamic response of steel-framed buildings by using additional braces and/or viscoelastic dampers. *Earthq. Eng. Struct. Dyn.* **2011**, *40*, 155–174. [CrossRef]
9. Kwag, S.; Gupta, A.; Baugh, J.; Kim, H.-S. Significance of multi-hazard risk in design of buildings under earthquake and wind loads. *Eng. Struct.* **2021**, *243*, 112623. [CrossRef]
10. Roy, T.; Saito, T.; Matsagar, V. Multihazard framework for investigating high-rise base-isolated buildings under earthquakes and long-duration winds. *Earthq. Eng. Struct. Dyn.* **2010**, *50*, 1334–1357. [CrossRef]
11. FEMA 356; Prestandard and Commentary for the Seismic Rehabilitation of Buildings. Federal Emergency Management Agency: Washington, DC, USA, 2010.
12. Fujimoto, M.; Wada, A.; Saeki, E.; Watanabe, A.; Hitomi, Y. A study on the unbonded brace encased in buckling-restraining concrete and steel tubes. *J. Struct. Constr. Eng.* **1988**, *34B*, 249–258. (In Japanese)
13. Fujimoto, M.; Wada, A.; Saeki, E.; Watanabe, A.; Hitomi, Y. A study on brace enclosed in buckling-restrained mortar and steel Tubes (Part 1). In *Annual Research Meeting Architectural Institute of Japan*; Architectural Institute of Japan: Tokyo, Japan, 1988. (In Japanese)
14. Fujimoto, M.; Wada, A.; Saeki, E.; Watanabe, A.; Hitomi, Y. A study on brace enclosed in buckling-restrained mortar and steel tubes (Part 2). In *Annual Research Meeting Architectural Institute of Japan*; Architectural Institute of Japan: Tokyo, Japan, 1988. (In Japanese)
15. Zhou, Y.; Shao, H.; Cao, Y.; Lui, E.M. Application of buckling-restrained braces to earthquake-resistant design of buildings: A review. *Eng. Struct.* **2021**, *246*, 112991. [CrossRef]
16. *International Building Code*; International Code Council: Washington DC, USA, 2024.
17. Holmes, J.D.; Bekele, S. *Wind Loading of Structures*, 4th ed.; CRC Press: Boca Raton, FL, USA, 2021. [CrossRef]
18. Kubo, Y. *Structure Configuration Based on Wind Engineering*, 2nd ed.; Chapter 13, Handbook of Structural Engineering; Chen, W.F., Lui, E.M., Eds.; CRC Press: Boca Raton, FL, USA, 2005.
19. Martinez-Vazquez, P. Wind design spectra for generalisation. *Wind. Struct.* **2020**, *30*, 155–163. [CrossRef]
20. Von Kármán, T. Progress in the statistical theory of turbulence. *Proc. Natl. Acad. Sci. USA* **1948**, *34*, 530–539. [CrossRef] [PubMed]
21. Davenport, A.G. The spectrum of horizontal gustiness near the ground in high winds. *J. R. Meteorol. Soc.* **1961**, *87*, 194–211. [CrossRef]
22. Harris, R.I. The nature of the wind. In *The Modern Design of Wind-Sensitive Structures*; Construction Industry Research and Information Association: Chicago, IL, USA, 1971.
23. Hino, M. Spectrum of gusty wind. In Proceedings of the Third International Conference on Wind Effects on Buildings and Structures, Tokyo, Japan, 26–28 February 1971; pp. 69–77.
24. Kaimal, J.C.; Wyngaard, J.C.; Izumi, Y.; Coté, O.R. Spectral characteristics of surface-layer turbulence. *J. R. Meteorol. Soc.* **1972**, *98*, 563–589. [CrossRef]
25. Simiu, E. Wind spectra and dynamic alongwind response. *J. Struct. Div.* **1974**, *100*, 1897–1910. [CrossRef]
26. Safak, E.; Foutch, D.A. *Vibration of Buildings under Random Wind Loads*; Civil Engineering Studies SRS-480; University of Illinois: Urbana-Champaign, IL, USA, 1980. Available online: <http://hdl.handle.net/2142/14087> (accessed on 1 July 2023).
27. Solari, G. Wind response spectrum. *J. Eng. Mech.* **1989**, *115*, 2057–2073. [CrossRef]
28. Jang, J.-J.; Lee, Y.-L. A study of along wind speed power spectrum for Taiwan area. *J. Mar. Sci. Technol.* **1998**, *6*, 2522. [CrossRef]
29. Mihanović, A.; Nikolić, Ž.; Smoljanović, H. Response spectrum of the Jugo wind force. *Int. J. Eng. Model.* **2008**, *1*, 33–41.
30. Kaimal, J.C.; Finnigan, J.J. Spectra and Cospectra Over Flat Uniform Terrain. In *Atmospheric Boundary Layer Flows*; Oxford University Press: Oxford, UK, 1994. [CrossRef]
31. SAC. SAC Steel Project Memorandum. 1994. Available online: <https://www.sacsteel.org> (accessed on 1 July 2023).
32. Menegotto, M.; Pinto, P.E. *Method of Analysis of Cyclically Loaded RC Plane Frames including Changes in Geometry and Non-Elastic Behavior of Elements under Normal Force and Bending*; Preliminary Report IABSE; IABSE: Manchester, UK, 1973; Volume 13.
33. Filippou, F.C.; Popov, E.P.; Bertero, V.V. *Effects of Bond Deterioration on Hysteretic Behavior of Reinforced Concrete Joints*; Report EERC 83-19; Earthquake Engineering Research Center, University of California: Berkeley, CA, USA, 1983.
34. Zsarnóczay, A.; Baker, J.W. Using model error in response history analysis to evaluate component calibration methods. *Earthq. Eng. Struct. Dyn.* **2020**, *49*, 175–193. [CrossRef]
35. Upadhyay, A.; Pantelides, C.P.; Ibarra, L. Residual drift mitigation for bridges retrofitted with buckling restrained braces or self centering energy dissipation devices. *Eng. Struct.* **2019**, *199*, 109663. [CrossRef]

36. Xu, W.; Pantelides, C.P. Strong-axis and weak-axis buckling and local bulging of buckling-restrained braces with prismatic core plates. *Eng. Struct.* **2017**, *153*, 279–289. [[CrossRef](#)]
37. *ANSI/AISC 341-22; Seismic Provisions for Structural Steel Buildings*. American Institute of Steel Construction: Chicago, IL, USA, 2022.
38. Kersting, R.A.; Fahnestock, L.A.; Lopez, W.A. *Seismic Design of Steel Buckling-Restrained Braced Frames: A Guide for Practicing Engineers*; National Institute of Standards and Technology: Gaithersburg, MD, USA, 2015; p. NIST GCR 15-917-34. [[CrossRef](#)]

Disclaimer/Publisher’s Note: The statements, opinions and data contained in all publications are solely those of the individual author(s) and contributor(s) and not of MDPI and/or the editor(s). MDPI and/or the editor(s) disclaim responsibility for any injury to people or property resulting from any ideas, methods, instructions or products referred to in the content.